JGR Atmospheres

RESEARCH ARTICLE
10.1029/2021JD036411

Special Section:
Southern Ocean clouds, aerosols, precipitation and radiation

Evidence for Secondary Ice Production in Southern Ocean Maritime Boundary Layer Clouds

Emma Järvinen[1,2], Christina S. McCluskey[1], Fritz Waitz[3], Martin Schnaiter[3,4], Aaron Bansemer[1], Charles G. Bardeen[1], Andrew Gettelman[1], Andrew Heymsfield[1], Jeffrey L. Stith[1], Wei Wu[5], John J. D'Alessandro[5,6], Greg M. McFarquhar[5,6], Minghui Diao[7], Joseph A. Finlon[8], Thomas C. J. Hill[9], Ezra J. T. Levin[9,10], Kathryn A. Moore[9], and Paul J. DeMott[9]

[1]National Center for Atmospheric Research, Boulder, CO, USA, [2]Now at Karlsruhe Institute of Technology, Karlsruhe, Germany, [3]Karlsruhe Institute of Technology, Karlsruhe, Germany, [4]schnaiTEC GmbH, Karlsruhe, Germany, [5]Cooperative Institute for Severe and High Impact Weather Research and Operations, University of Oklahoma, Norman, OK, USA, [6]School of Meteorology, University of Oklahoma, Norman, OK, USA, [7]Department of Meteorology and Climate Science, San Jose State University, San Jose, CA, USA, [8]Department of Atmospheric Sciences, University of Washington, Seattle, WA, USA, [9]Department of Atmospheric Science, Colorado State University, Fort Collins, CO, USA, [10]Now at Handix Scientific, Boulder, CO, USA

Abstract Maritime boundary-layer clouds over the Southern Ocean (SO) have a large shortwave radiative effect. Yet, climate models have difficulties in representing these clouds and, especially, their phase in this observationally sparse region. This study aims to increase the knowledge of SO cloud phase by presenting in-situ cloud microphysical observations from the Southern Ocean Clouds, Radiation, Aerosol, Transport Experimental Study (SOCRATES). We investigate the occurrence of ice in summertime marine stratocumulus and cumulus clouds in the temperature range between 6 and −25°C. Our observations show that in ice-containing clouds, maximum ice number concentrations of up to several hundreds per liter were found. The observed ice crystal concentrations were on average one to two orders of magnitude higher than the simultaneously measured ice nucleating particle (INP) concentrations in the temperature range below −10°C and up to five orders of magnitude higher than estimated INP concentrations in the temperature range above −10°C. These results highlight the importance of secondary ice production (SIP) in SO summertime marine boundary-layer clouds. Evidence for rime splintering was found in the Hallett-Mossop (HM) temperature range but the exact SIP mechanism active at lower temperatures remains unclear. Finally, instrument simulators were used to assess simulated co-located cloud ice concentrations and the role of modeled HM rime-splintering. We found that CAM6 is deficient in simulating number concentrations across the HM temperature range with little sensitivity to the model HM process, which is inconsistent with the aforementioned observational evidence of highly active SIP processes in SO low-level clouds.

Plain Language Summary Clouds in the Southern Ocean are important for climate but not well represented in climate models. Observations in this remote region have been rare. This study presents results from a recent airborne campaign that took place in the Southern Ocean where low- and mid-level clouds were investigated by detecting individual cloud particles within the clouds. Although large fraction of the observed clouds did not contain ice crystals, occasionally high amounts of ice crystals were observed that cannot be explained by ice formation on aerosol particles but were result of multiplication of existing ice crystals. We tested the capability of a commonly used climate model to represent the observed ice concentrations and their sensitivity to one ice multiplication process parameterized in the model. These investigations revealed that the in the model the ice multiplication process was not responsible for generation of ice, which is in contradiction with the observations.

Key Points:

- Ice concentrations several orders of magnitude higher than ice nucleating particle concentrations were observed
- Secondary ice production was believed to be responsible for the observed high ice number concentrations
- Comparison with climate model indicated that secondary ice processes are still inadequately represented in the model

Supporting Information:

Supporting Information may be found in the online version of this article.

Correspondence to:

E. Järvinen,
emma.jaervinen@kit.edu

Citation:

Järvinen, E., McCluskey, C. S., Waitz, F., Schnaiter, M., Bansemer, A., Bardeen, C. G., et al. (2022). Evidence for secondary ice production in southern ocean maritime boundary layer clouds. *Journal of Geophysical Research: Atmospheres*, *127*, e2021JD036411. https://doi.org/10.1029/2021JD036411

Received 27 DEC 2021
Accepted 17 JUL 2022

© 2022. The Authors.
This is an open access article under the terms of the Creative Commons Attribution License, which permits use, distribution and reproduction in any medium, provided the original work is properly cited.

1. Introduction

The Southern Ocean (SO) is one of the cloudiest regions in the world with fractional cloud cover commonly exceeding 80% (i.e., Mace et al., 2007; Mace & Zhang, 2014; Muhlbauer et al., 2014). Maritime boundary layer clouds in the SO have a significant shortwave (SW) cloud radiative effect associated with them (Haynes et al., 2011), and consequently they have an important role when estimating climate sensitivity to cloud feedbacks

Table 1
List of Previous Campaigns Over the SO Region Where Mixed-Phase Clouds Were Measured

Campaign	Reference	Location	Time	Cloud T	$N_{droplets}$	max N_{ice}
	Huang et al. (2017), Ahn et al. (2017)	Southwest coast of Tasmania	Jun-Oct 2013–2015	9.1 to −18.7°C	28 ± 30 cm^3	54 L^{-1} [a]
MAC	O'Shea et al. (2017)	Coastal Antarctica and the Weddell Sea	Austral summer 2015	−3 to −11°C	113 cm^3	50 L^{-1} [b]
HIPPO	Chubb et al. (2013)	South of Australia	Nov 2009 and Apr 2010	−11 to −22°C	30–120 cm^3	0.4 L^{-1} [c]
ACE 1	Boers and Krummel (1998)	South of Tasmania	Nov-Dec 1995	*	45–200 cm^3	Observed but not quantified
SOCEX	Boers et al. (1996); Boers et al. (1998)	West of Tasmania	Jul 1993 (SOCEX I) Jan-Feb 1995 (SOCEX II)	*	50 cm^3 (Winter) 180 cm^3 (Summer)	Observed but not quantified
	Mossop (1985)	Coast of Tasmania	June 1981	5 to −10°C	80–410 cm^3	350 L^{-1} [d]
	Mossop et al. (1970)	Coast of Tasmania	May 1968	5 to −17°C		∼100 L^{-1} [e]
	Mossop et al. (1968)	Southern coast of Australia	17 Oct 1966	3 to −4.5°C	100 cm^3	∼100 L^{-1} [e]

*Information not available. [a]7.9.2013 case study. [b]Only ice particles D_{max} > 80 μm. [c]Only ice particles D_{max} > 100 μm. [d]Only ice particles D_{max} ∼ > 150 μm. [e]Derived from replicator measurements.

(Trenberth & Fasullo, 2010). Large biases in the SW radiation budget over the SO were present in many CMIP5 models (Coupled Model Intercomparison Project Phase 5) (Bodas-Salcedo et al., 2012; Kay et al., 2016; Trenberth & Fasullo, 2010). Later, these biases have been improved in Phase 6 models (CMIP6) through various means to generate more supercooled liquid over the SO region (Bodas-Salcedo et al., 2019; Gettelman et al., 2019). With modeling studies that highlight the potential importance of the cloud phase feedback over the SO for global climate (Bjordal et al., 2020), it is important for CMIP6 models to correctly represent the microphysical processes that govern the state of SO cloud phase.

Our understanding of SO microphysical processes and cloud phase have been restricted due to the remoteness of the region. Although space-borne remote sensing retrievals of the SO cloud phase are valuable, these are limited in numerous ways. For example, Mace and Protat (2018) found large discrepancies between satellite and ship-based remote sensing observations of the cloud phase, with a larger occurrence of ice phase found by the latter method. This bias was partly caused by the inability of space-borne lidar observations to probe more than a few optical depths into the tops of the clouds, missing ice-processes taking place deeper in the vertical column.

In supercooled liquid clouds the first ice crystals are generated through primary nucleation, where ice is formed on aerosol particles that are called ice nucleating particles (INPs). In the pristine SO region, the number of INPs is too low (McCluskey et al., 2018) to completely explain the glaciation of low level clouds. Multiplication of frozen hydrometeors is possible through secondary ice processes (SIP). These processes are found to be responsible to generate orders of magnitude higher ice number concentrations than expected by primary nucleation (P. R. Field et al., 2017; A. Korolev et al., 2020; A. Korolev & Leisner, 2020, and references therein). The role of INPs and SIP to generate ice in SO clouds have been experimentally studied by airborne in-situ observations since the 1960s (Mossop et al., 1968; Mossop et al., 1970, and Table 1). The early airborne studies reported ice particle concentrations as high as 100 L^{-1} in cumulus clouds at temperatures warmer than −17°C, well exceeding the simultaneously measured or estimated INP concentrations, and providing the first evidence of SIP in the region. These studies acted as the motivation for later laboratory studies by Hallett and Mossop (Hallett & Mossop, 1974).

The Hallett-Mossop (HM) ice multiplication process is one of the most studied SIP processes. In summary, the HM process takes place in the temperature region approximately between −2 and −8°C in the presence of liquid droplets larger than 24 μm in diameter that can freeze when collected by larger ice particles. Mossop (1985) found that HM process was active in all days the authors were measuring in wintertime cumuli at the coast of Tasmania in June 1981. More recently, Huang et al. (2017) reported ice concentrations up to 54 L^{-1} at temperatures warmer than −9°C in SO open cellular convection and O'Shea et al. (2017) reported similar ice particle number concentrations in coastal Antarctic clouds during the MAC campaign.

Airborne in-situ observations in SO stratocumulus clouds have been performed since 1990s (Boers et al., 1996, 1998; Boers & Krummel, 1998; Chubb et al., 2013). Unlike the studies of cumulus clouds, these campaigns reported mostly liquid phase clouds (see Table 1). Ice crystals were observed occasionally but their concentrations were either not reported or they were found to be low, below 0.4 L^{-1} (Chubb et al., 2013), giving no evidence for active SIP. However, it should be noted that characterizing the cloud phase was not the main objective of these studies, and therefore, the instrumentation for detecting ice crystals was limited.

Furthermore, there has been an increasing effort by the modeling community to understand SIP in SO clouds in recent years. Young et al. (2019) was the first to show that a widely-used description of the HM process using an empirically derived splinter production rate cannot reproduce the ice crystal concentrations in stratocumulus clouds observed during the MAC campaign (see Table 1). However, including a parameterization for SIP due to mechanical breakup from collisions between ice particles improved the representation of the observed ice crystal concentrations (Sotiropoulou et al., 2021). Atlas et al. (2020) showed that the CESM Community Atmosphere Model (CAM6) was insufficient in reproducing the observed large particle modes ($D > 200$ μm) assumed to be frozen particles in SO clouds occupying the HM temperature range. The performance of the CAM6 model was significantly improved when droplet shattering during freezing of rain and ice-ice collision fragmentation SIP mechanisms were included (Zhao & Liu, 2021). The authors also highlighted the dominant role of SIP in formation of ice in moderate cold clouds in the southern hemisphere.

Despite previous efforts, comprehensive understanding of SO cloud phase has not been reached. Here we aim to improve the knowledge of SO clouds by presenting in-situ observations from the Southern Ocean Clouds, Radiation, Aerosol, Transport Experimental Study (SOCRATES) experiment (McFarquhar et al., 2021) that operated a suite of instruments for characterization of the ice phase, including a newer cloud probe for detection of small ice. We report ice crystal number concentrations in stratocumulus and cumulus clouds covering a wide temperature range from +3 to −25°C and discuss these in conjunction with co-located INP measurements. Additionally, the observed ice number concentrations are compared with simulated number concentrations from a series of global climate model simulations using the CAM6 model targeted toward assessing a commonly used numerical representation of SIP (Cotton et al., 1986). Here, we introduce a novel approach to use instrument simulators to take into account the probe performance when comparing the observations to the simulations. Section 2 describes the instrumentation and methodology used to derive ice particle and INP number concentrations as well as the model and its configuration. Section 3 discusses the cloud types included in this study. The observational results are shown in Sections 4 and 5 and a discussion of the findings in conjunction with potential SIP processes is given in Section 6. The model results are discussed in Section 7 and a summary is given in Section 8.

2. Data and Methodology

During the austral summer, from January 15 to February 26 in 2018, research flights targeting SO maritime and boundary layer clouds mainly in the cold dry sector of cyclones were made using the NSF/NCAR High-performance Instrumented Airborne Platform for Environmental Research (HIAPER) aircraft between Hobart, Tasmania and 62°S. Altogether 15 research flights were conducted, of which 13 flights investigated stratocumulus and two flights targeted cumulus systems. In this paper, we present data from the second research flight (RF02) to the last research flight (RF15), as cloud particle stereo-microscopic images were not available from RF01. The flight strategy included a transit leg at approximately 6 km directly to the southern-most point of the flight followed by a descent to perform repeated above-, in-, and below-cloud level leg maneuvers augmented by a series of sawtooth profiling patters while traveling north toward Hobart (Figure 1). Clouds were only sampled once to avoid ”contaminating” the measurements with aircraft-produced ice particles (Sassen, 1991; Woodley et al., 2003).

The HIAPER aircraft was equipped with a range of in-situ and remote sensing instruments (UCAR/NCAR - Earth Observing Laboratory [EOL], 2018) for characterization of cloud and aerosol microphysical, optical and radiative properties as well as instrumentation to measure navigation and state parameters (UCAR/NCAR - Earth Observing Laboratory [EOL], 2019b). A complete list of instruments as well as more detailed description of the flight strategy can be found in McFarquhar et al. (2021). Here, we give an overview of the measurements relevant for this study, followed by a description of the global climate model used to simulate the SOCRATES observations.

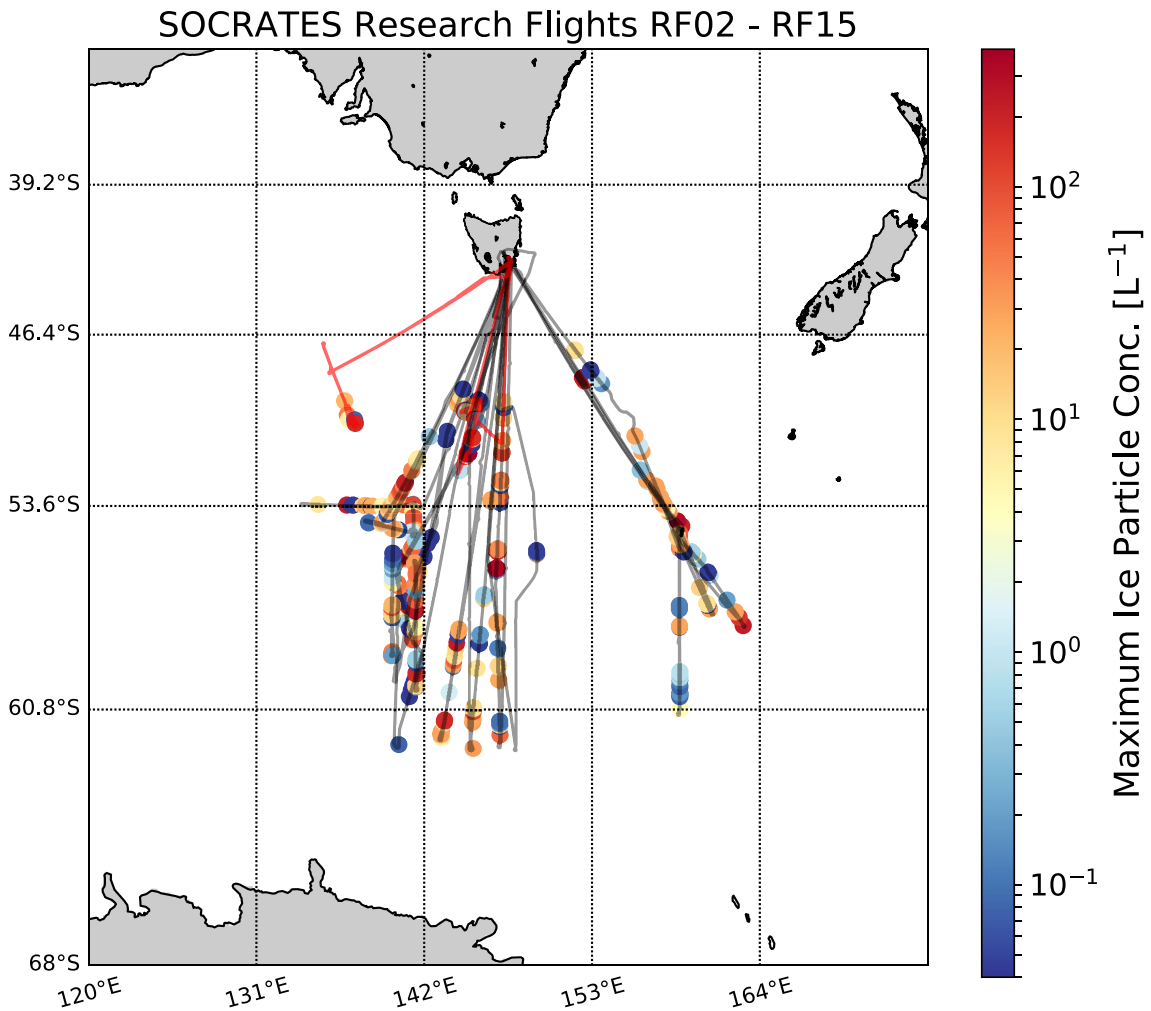

Figure 1. HIAPER flight tracks of SOCRATES research flights RF02 to RF15. The flight tracks of missions targeting stratocumulus systems are shown in black and the flight tracks of missions targeting cumulus systems in red. Ice detected in cloud passes on the return legs are shown as dots and colored by the maximum number concentration, illustrated by the color bar. The cloud passes are defined in Table S1 in Supporting Information S1. Note that each research flight composed of a transit leg to the southernmost point followed by a descent to perform in-situ sampling while traveling north toward Hobart so each cloud system was only sampled once.

2.1. Temperature and Relative Humidity Measurements

The ambient temperature was measured with a heated temperature sensor (Harco Model 100009-1 Deiced TAT) that has a general accuracy of 0.2–0.3°C (UCAR/NCAR - Earth Observing Laboratory [EOL], 2019b). The water vapor mixing ratio was measured with the Vertical-Cavity Surface-Emitting Laser (VCSEL) hygrometer (Diao, 2021). Relative humidity with respect to water (RH) was calculated from temperature, pressure and water vapor mixing ratio measurements using Murphy and Koop (2005) parameterization for saturation vapor pressure. Water vapor number concentration uncertainty of the VCSEL hygrometer was generally about 6% in SOCRATES. Combined with the temperature uncertainty, the resulting uncertainty of RH can range from 6% to ~10%. In particular, for temperatures around −5°C when SIP tends to occur relatively frequently (e.g., Lukee, 2021), the measurement of VCSEL is often switching between two modes—the weak and direct modes. During the case studies of RF12 and RF09 selected in this work (as shown in Section 5), constant mode switching of VCSEL was seen, while laser intensity also decreased significantly possibly due to icing. Both mode switching and low laser intensity can lead to larger uncertainty in the water vapor measurements, which may be the main reasons for deviations of RH from liquid saturation seen in these time series.

2.2. Liquid Water Content and Droplet Size Spectrum

The cloud microphysical instruments onboard the HIAPER included the forward scattering Cloud Droplet Probe (CDP, Droplet Measurement Technologies, USA) for measurements of primary cloud droplets in the diameter (D) range from 2 to 50 μm (UCAR/NCAR - Earth Observing Laboratory [EOL], 2019b). The average uncertainty of the CDP measurements in sizing is around ∼30% and in number concentrations between 10 and ∼30% (Baumgardner et al., 2017). Liquid water content (LWC) was estimated from the CDP measurements through the integration of cloud droplet size distributions.

2.3. Ice Crystal Measurements

For characterization of the ice phase during SOCRATES a combination of the Particle Habit Imaging and Polar Scattering (PHIPS) probe (Abdelmonem et al., 2016; Schnaiter et al., 2018; Waitz et al., 2021) and the 2D-S (SPEC Inc., USA, R. P. Lawson et al. (2006)) was used. PHIPS is a single-particle polar nephelometer and stereo-microscopic cloud particle imager that detects ice particles in the area equivalent diameter (D_{eq}) range from 30 to 700 μm. The angular scattering function of individual cloud particles is detected with a maximum repetition rate of 3.5 kHz whereas the maximum data acquisition rates of the cameras were set to 3 Hz so only a subset of triggered cloud particles were imaged. The stereo-microscopic imager part of the PHIPS can be operated with different magnification settings that define the optical resolution and image field-of-view. During SOCRATES the magnification was chosen so that the optical resolutions was between ∼6.8 μm and ∼6.2 μm.

The 2D-S records shadowgraphs of cloud particles that are used to determine particle size distributions (PSDs), condensed water content (CWC), ice water content (IWC) and particle shape properties of liquid- and ice-phase cloud hydrometeors (Wu & McFarquhar, 2019b). The 2D-S has an optical resolution of 10 μm and it nominally measures cloud particles with maximum dimension ($D_{\max}$) from 0.01 to 3.2 mm. The 2D-S data were processed using the University of Illinois/Oklahoma optical array probe (OAP) Processing Software (UIOOPS, McFarquhar et al. (2018)), which determines morphological features (e.g., maximum dimension, area equivalent diameter, area ratio, habit) of individual cloud hydrometeors. CWC and IWC were calculated for particles consisting of four or more pixels using the habit-dependent mass-dimension relationships (Wu & McFarquhar, 2016) or the mass to area relationship from Baker and Lawson (2006).

Additionally, a NCAR modified version of the 2DC (PMS Inc., USA) was operated during SOCRATES. However, the 2DC encountered some operational issues during the campaign, which reduced confidence in the data quality. Therefore, the 2D-S was primarily used to get information on cloud hydrometeors, except for RF15 when 2D-S data was not available for the majority of the flight. The performance of 2DC is compared to 2D-S in the supplementary material for the part of RF15 where both probes were operational.

2.3.1. Identification of Non-Spherical Particles

It has been shown that the shape of the angular scattering function of individual cloud hydrometeors is sensitive to the particle shape (Järvinen et al., 2016; Schnaiter et al., 2018). PHIPS single-particle polar nephelometer measurements were used to discriminate between spherical and aspherical particles in the particle diameter range $D_{eq} < 200$ μm. A detailed description of this phase discrimination method can be found in Waitz et al. (2021). The authors showed that, for the SOCRATES data set, the probability of misclassifying a droplet as an ice crystal is 4.2%, whereas the probability of misclassifying an ice crystal as droplet is only 0.3% for the diameter range $D_{eq} = 60$–700 μm. In the diameter range $D_{eq} < 60$ μm PHIPS only triggers on aspherical particles due to its trigger geometry (Schnaiter et al., 2018).

Non-spherical particles were identified from the 2D-S shadowgraphs using the habit classification algorithm of Holroyd (1987). Holroyd (1987) identifies particle sphericity using a combination of particle shape and surface roughness where the latter is quantified using the fine detail ratio, defined as the perimeter multiplied by maximum dimension and divided by projected area. Altogether nine habits are defined for frozen hydrometeors. There are no studies quantifying the uncertainty in Holroyd habit classification and in this study we have considered the method to be accurate for particle diameters $D_{eq} \geq 200$ μm.

2.3.2. Deriving Ice Concentrations in the Diameter Range From 30 to 1,600 μm

Here, ice crystal number concentration is defined as the number concentration of aspherical particles. The number concentration of aspherical particles for D_{eq} range from 30 to 200 μm was derived using PHIPS single particle angular scattering data (Schnaiter, 2018) following the method presented in Waitz et al. (2021) but with the exception that the sensitive volume was calculated differently. Waitz et al. (2021) showed that the PHIPS sensitive area shows a strong exponential dependency to particle diameter for small particles with $D_{eq} < 100$ μm and this dependency becomes weaker as the particle diameter increases. To take into account the stronger diameter dependency of the sensitive area for small particles, we calculated for each detected particle a unique sensitive volume and set the bin sensitive volume to be the mean of the individual sensitive volumes for a given time step instead of using a fixed sensitive volume for each bin as was done in Waitz et al. (2021). We also considered only particles with $D_{eq} \geq 30$ μm in this study to reduce uncertainties in the small particle concentrations caused by strong decrease in the sensitive area at sizes close to the detection limit.

PHIPS ice crystal number concentrations were calculated with a time resolution of 10 s, which corresponds to a sampling volume of ∼270 cm^3 at an airspeed of 150 $m\,s^{-1}$ and a minimum detectable concentration of ∼3 L^{-1} in a 10-s interval. Thermodynamic correction was applied according to Weigel et al. (2016) to take into account the compression of air occurring upstream of the air flow obstacle provided by the instrument's body. Occasionally, ice particle shattering on the probe head affected the measured concentrations. The shattering influenced periods were identified as periods when large ($D_{eq} > 800$ μm) ice crystals were present in number greater than 10% of the total number concentration as seen by the OAPs (see detailed discussion of shattering events during SOCRATES in Waitz et al. (2021)). This entailed about 23% of the 10 s in-cloud data (with half of the events being at temperatures colder than −11°C). For these periods, PHIPS data was not used and ice crystal number concentrations are only given for particles with $D_{eq} \geq 200$ μm.

The number concentration of aspherical particles for the size range $D_{eq} \geq 200$ μm was derived from the 2D-S (Wu & McFarquhar, 2019a). The uncertainty in the 2D-S sizing and number concentrations for particles with $D > 100$ μm has been evaluated to be ∼20% and ∼50%, respectively (Baumgardner et al., 2017). Only particles having their center within the OAP field of view were included (Heymsfield & Baumgardner, 1985; P. R. Field, 1999). The 2D-S probe was equipped with anti-shattering tips to reduce shattering artifacts. However, a shattering removal algorithm (Jackson & McFarquhar, 2014; P. Field et al., 2006) was used to further eliminate shattering influenced periods. The number concentrations were originally given in a time resolution of 1 Hz but we averaged the samples over 10-s periods to be comparable to the PHIPS data. These periods correspond to a sampling volume of 120 L at an airspeed of 150 $m\,s^{-1}$ for particles with $D_{eq} \geq 200$ μm and a minimum detectable concentration of ∼0.008 L^{-1} in a 10-s interval.

Figure 2 shows particle size distributions (PSDs) for all particles and for aspherical particles derived from PHIPS and 2D-S as a function of D_{eq} for a liquid-dominated mixed-phase cloud. Almost all the cloud particles with $D_{eq} \geq 200$ μm were found to be aspherical whereas smaller particles were primarily spherical. In the $D_{eq} < 200$ μm range the PHIPS can discriminate aspherical particles from the dominating mode of spherical particles. In the instrument overlap region ($200 \geq D_{eq} < 700$ μm) the concentrations of aspherical particles retrieved from PHIPS and 2D-S agree within the statistical uncertainty of the instruments. For the size range ($D_{eq} \geq 700$ μm) all the particles detected by the 2D-S were aspherical.

To calculate the total ice number concentrations a combination of PHIPS and 2D-S measurements for different D_{eq} ranges was used. For $D_{eq} < 200$ μm concentration of aspherical particles from PHIPS was used for segments not affected by shattering. For $D_{eq} \geq 200$ μm the concentration of aspherical particles from 2-DS was used. Note that in this study 2D-S sizing was based also on D_{eq} instead of $D_{\max}$. The threshold diameter of 200 μm was based on the lower limit where 2D-S phase discrimination was considered to have a high degree of confidence, since given the optical resolution of 2D-S, morphological properties are better resolved for habit ID applications with increasing particle size. Total ice number concentrations are given with the time resolution of 10 s to allow sufficient sampling statistics. The detection limit for the 10-s samples depends now on the particle size. For $D_{eq} \geq 200$ μm the detection limit is defined by the 2D-S detection limit, which is 0.008 L^{-1}, but smaller particles with $D_{eq} < 200$ μm can be only detected if their concentration is above 3 L^{-1}.

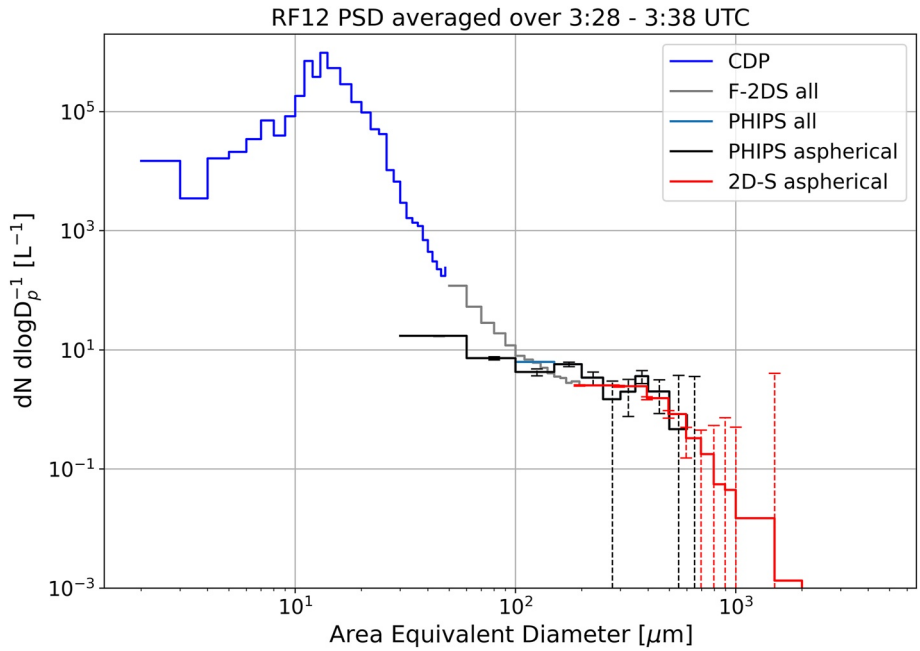

Figure 2. PSDs averaged for a 10 min period during sampling of a mixed-phase cloud with a mean temperature around −6°C. Dashed bars illustrate the statistical uncertainty of the measurements for aspherical particles. Note that "PHIPS all" only includes particles with $D_{eq} > 100$ µm since spherical particles below 60 µm are not detected and between 60 and 100 µm are under-sampled.

2.4. INP Filter Measurements Onboard HIAPER

Aerosol particles were collected onto filters and analyzed with the Colorado State University (CSU) Ice Spectrometer (IS) to determine number concentrations of immersion freezing INPs at temperatures from 0 to approximately −28°C.

The filter sample collection approach used in this study follows that of previous aircraft studies (Levin et al., 2019; Twohy et al., 2016) and is described briefly here. Particles were collected onto pre-cleaned 0.2 µm-pore-diameter Nuclepore polycarbonate membranes (Whatman), each overlying a pre-cleaned 8 µm-µm-pore-diameter Nuclepore polycarbonate backing membrane (to avoid any potential contamination of INPs from the support grid). These were fitted into sterilized 47-mm diameter in-line aluminum filter holders. Cleaning procedures for filters included a 10% H_2O_2 rinse, three rinses in filtered (0.01 µm pore diameter) deionized water, and drying on foil in a laminar flow cabinet, following previous studies (McCluskey et al., 2017). Anodized aluminum filter holders were cleaned, using 3%–6% H_2O_2 and deionized water rinses and stored in a clean plastic tub for drying, and reassembled for each research flight.

Samples during SOCRATES were collected as "above cloud" or "below cloud" measurements during clear-air level legs from a HIAPER modular aerosol inlet (Stith et al., 2009), using a plumbing system that allowed for continuous bypass flow to two filter units that could be alternately opened to or isolated from sampling flow at varied times. Filters were exposed for approximately 10 min during level legs above or below cloud. To increase sampling volume and therefore improve detection limit, samples were exposed for 1–3 level legs per flight in each region, representing a range of latitudes. Each flight consisted of a minimum of one above and one below cloud filter. 32 filter samples were collected during SOCRATES and total sample volumes per flight ranged from 129 to 840 standard liters of air, with a median volume of 352 standard liters, as monitored by a mass flow meter. After collection, filters were removed and stored in INP-free plastic petri dishes (CELLTREAT) at −20°C and shipped back to CSU in a liquid nitrogen shipper (Cryoport). Six blank filters were collected over the course of the study, by placing a prepared filter unit in place without flow during flight, to quantify INP contaminants introduced during the cleaning, storage, and handling procedures.

At CSU, samples were analyzed following procedures described by Hill et al. (2016), including re-suspension of particles from filter samples into six or 7 mL of 0.02 µm-filtered deionized water and distribution in 50 µL aliquots that were monitored for freezing during cooling at 0.33°C min^{-1} in the IS. INP number concentrations per suspension volume were obtained as a function of temperature for each filter sample after correction for the regression mean from blank filters, then converted to INP per standard liter of air using the sample volumes (Hiranuma et al., 2015). This resulted in lower detection limits than actually measured, that ranged between 0.0035 and −0.03 L^{-1} depending on the sample volume. Confidence intervals (95%) were calculated for binomial sampling. Only composite results from all samples will be discussed in this manuscript.

2.5. Model Simulations

Observations from SOCRATES were used to assess clouds simulated by the Community Atmospheric Model versions 6 (CAM6), which is the atmospheric component of the Community Earth System Model version 2 (Danabasoglu et al., 2020). Simulations for the SOCRATES field campaign are described in detail by Gettelman et al. (2020) and are described briefly here.

CAM6 uses a 2-moment cloud microphysics scheme that prognoses 4 classes of hydrometeors (liquid, ice, rain, and snow) (Gettelman and Morrison (2015); Gettelman et al. (2015)). CAM6 includes the dust heterogeneous ice nucleation scheme from Hoose et al. (2010) to determine immersion, deposition, and contact freezing rates in mixed phase clouds. CAM6 also includes modifications to the Hoose et al. (2010) scheme for a distribution of contact angles (Wang et al., 2014) and accounts for preexisting ice in the cirrus ice nucleation of Liu and Penner (2005) as described by Shi et al. (2015). Immersion freezing of dust aerosol is active for temperatures lower than −10°C in CAM6. Note that this scheme does not include sea spray aerosol that is a major source of INPs in the SO region (McCluskey et al., 2018, 2019). Secondary ice production through the Hallet-Mossop (HM) rime-splintering process is represented following a parameterization from Cotton et al. (1986); simulated rimed mass is multiplied by an ice multiplication rate that maximizes at −5°C and linearly decreases to zero at −3°C and −8°C. Detailed comparison between CAM6 simulations and in-situ measured (Dropsonde) temperatures and winds are shown in Gettelman et al. (2020).

In this study, CAM6 simulations used the standard 32 vertical levels from the surface to 3 hPa, 0.9° latitude by 1.25° longitude horizontal resolution, and 30 min time resolution. Simulations were performed in a 'nudged', or specified dynamics, configuration over the SOCRATES study period. Specifically, model winds and temperatures are relaxed to reanalysis data from the NASA Modern-Era Retrospective analysis for Research and Applications, version 2 (MERRA2), with a 24-hr relaxation period.

A base simulation (*CAM base*) was performed with default physics for initial comparisons. To investigate the role of HM ice multiplication on simulated SOCRATES clouds in CAM6, the ice multiplication rates in CAM6 were (a) reduced to zero at all temperatures (*CAM HMoff*) or (b) increased by a factor of five across all HM temperatures (*CAM HMx5*). We note that simulated ice number concentrations in the CESM2 release version of CAM6 are limited by an ice number limiter that constrains ice number if the simulated ice number concentration reaches the number specified by the ice nucleation scheme. This limiter is intended to prevent heterogeneous ice formation if the simulated ice number concentrations exceed predicted ice nuclei concentrations, which may arise due to the model timestep. In this work, we focus on assessing simulated ice number concentrations and simulated sensitivity to the HM process in the CESM2-CAM6 release model configuration used in Gettelman et al. (2020), which does include this limiter. Shaw et al. (2022) have highlighted this as a controlling feature on cloud properties, especially in the mixed phase cloud regime, because the ice number rates from Hoose et al. (2010) were not included in the limiter. Shaw et al. (2022) notes this ice number limiter is un-intentionally low. We expect the ice number limiter dampens the simulated sensitivity to the parameterized HM process and we will test this with a sensitivity test of a developmental model version without the limiter.

3. Cloud Types Analyzed

In this study, we are concerned with low- and mid-level layer clouds with varying degrees of weak vertical motions and generating cells. Our analysis includes only cloud sample periods (cloud segments) that included a minimum of 10 s of in-cloud conditions, defined as a 1-Hz-period where the CWC values were >0.001 g m^{-3} (e.g., McFarquhar et al., 2007; McFarquhar et al., 2021), and where the minimum in-cloud temperature was below

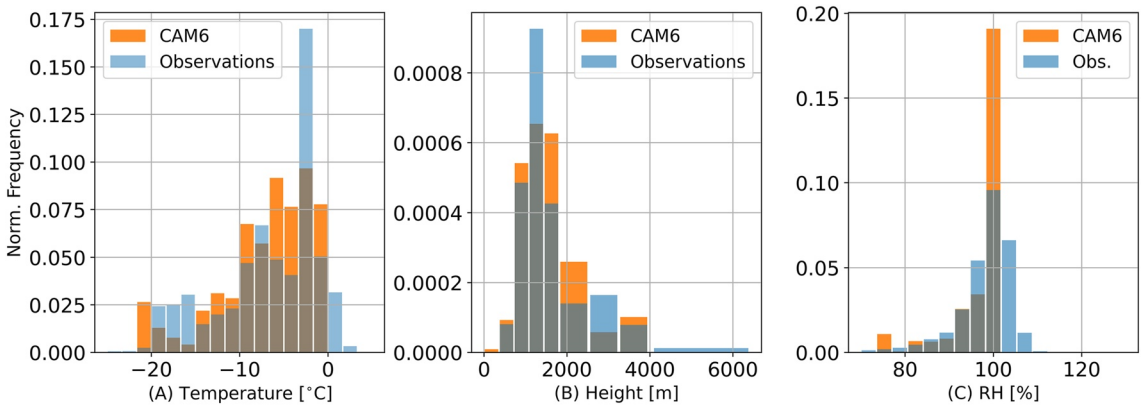

Figure 3. Relative frequency histogram of observed and simulated values for in-cloud temperature, height and RH with respect to water for stratocumulus cloud segments as defined in Table S1 in Supporting Information S1. The normalization is performed so that the area under the histogram integrates to 1. Observations are based on 1-Hz values.

freezing point so that ice can form either though primary ice nucleation or through SIP. Furthermore, clouds sampled during transit legs at 6 km were not considered. This resulted in 385 cloud segments in stratocumulus clouds and 34 cloud segments in cumulus clouds sampled in the geographical area between −42.5°S and −62.1°S (Figure 1). Individual cloud segments were detected for periods between 10 s and 18 min. In total, 7 hr of data in stratocumulus clouds and 10 min of data in cumulus clouds is reported with a total lengths in clouds of 3,444 km and 78 km, respectively.

The homogeneous stratocumulus cloud fields were sampled along a straight line toward Hobart from the southernmost way point (see Figure 1) so sampling can be considered unbiased (P. R. Field & Furtado, 2016). Cumulus sampling strategy required active decisions on which system to sample, which could lead to bias toward more matured cumulus towers.

Figure 3 shows the relative frequency histograms of observed and simulated values for in-cloud temperature (Figure 3a), height (Figure 3b) and RH (Figure 3c) for the stratocumulus cloud segments. Most of the observed stratocumulus clouds were low-level clouds found below 2 km, which resulted in a peak in the observed in-cloud temperatures between 0 and −10°C. In order to investigate the possible effects of seeding, multi- and single-layered systems were manually classified by inspection of radar and lidar data as well as looking at the camera imagery obtained onboard the HIAPER (UCAR/NCAR - Earth Observing Laboratory [EOL], 2019a). An example classification can be seen in Figures S2 and S3 in Supporting Information S1. This classification was possible in 360 (out of 385) cloud segments. Altogether, 243 cloud segments were classified as multi-layer systems, whereas 117 were classified as single-layer systems.

During RF11 and RF15, cumulus systems were targeted, where single passes were made through developing small cumuli south of Hobart (RF11) and southwest of Hobart (RF15) between −49 and −52°S (Figure 1). Here, 34 of these passes were analyzed for their ice crystal concentrations. The minimum temperatures during the segments varied between −0.5 and −9.3°C. For a more detailed discussion of cumulus systems in SOCRATES we refer to Lasher-Trapp et al. (2021).

4. Results

4.1. Ice Crystal Number Concentrations and Evidence for Secondary Ice Production

Ice crystal concentrations above the detection limit were observed on average during 33% of the cloud segments and during 55% of the 10-s samples. For a more detailed discussion of the relative frequency of cloud phases we refer to D'Alessandro et al. (2021). Figure 4 shows the 10-s average ice crystal number concentrations (n_{ice}) for these samples as a function of temperature. It can be seen that n_{ice} varies over several orders of magnitude for both cumulus and stratocumulus clouds, consistent with previous measurements of SO clouds (Table 1). The highest 10-s n_{ice} values were found around −5°C with a 95th percentile n_{ice} of 69 L^{-1} and mean n_{ice} of 9.8 L^{-1}. The median n_{ice} over all sampling periods was 0.04 L^{-1} (including periods with ice concentrations below the detection limit).

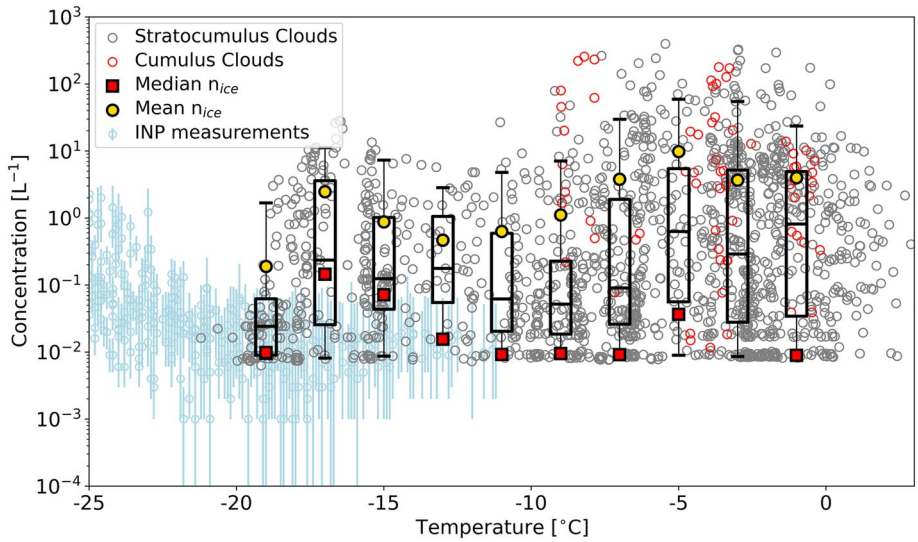

Figure 4. Observed ice particle number concentrations averaged over 10-s periods as a function of local in-cloud temperature for the investigated stratocumulus (gray) and cumulus (red) cloud segments. Statistical analysis ice concentrations above the detection limit in 2°C temperature bins are shown as box-plots where the box center line, box edges and whiskers represent the median, interquartile range and 5%–95% range, respectively. The red squares (yellow dots) show the median (mean) values of all data points, including time periods when ice number concentration was below the detection limit. The median value for the size bin between −2 and −4°C is zero and therefore not shown in the figure. Note that the detection limit of ∼0.008 L^{-1} is defined through the 2D-S sampling volume and is only valid for ice crystals larger than 200 μm. Measurements of INPs from the HIAPER taken both below and above the sampled clouds are shown in light blue circles with 95% confidence intervals shown as vertical lines. Note that the INP measurements represent a minimum sampling time of 10 min and thus represent a different spatial scale compared to the ice observations. The total length of sampled clouds was 3,524 km.

The highest median n_{ice} of 0.15 L^{-1} was observed between −16 and −18°C with a 95th percentile n_{ice} of 11 L^{-1}. However, colder temperatures covered fewer observations and concentrations >1 L^{-1} came from nine profiles on three research flights (RF03, RF09, and RF10). The lowest n_{ice} were observed around −10°C.

The observed median ice crystal number concentrations during SOCRATES were on average lower than what is observed in the Arctic (e.g., Hobbs & Rangno, 1998; Lloyd et al., 2015; McFarquhar et al., 2007; Mioche et al., 2017; Rangno & Hobbs, 2001) but similar to what was observed previously in summer time coastal Antarctic clouds during the MAC campaign (O'Shea et al., 2017). During MAC a similar peak in n_{ice} around −6°C was observed (O'Shea et al., 2017; Young et al., 2019). Other studies in the region have also reported n_{ice} of up to several tens per liter at temperatures greater than −10°C (see Table 1).

To investigate possible ice formation pathways, INP concentrations (n_{INPs}) measured in clear air above and below cloud layers between cloud sampling periods are provided in Figure 4. Here, n_{INPs} can correspond to the n_{ice} if ice is only formed via the immersion freezing process. It should be also noted that in Figure 4 n_{ice} is given as a function of local cloud temperature but the relevant n_{INPs} value should be considered to be the value corresponding to cloud top temperature. Since the sampled clouds were shallow, the difference between local temperature and cloud top temperature would be less than 10°C.

The maximum n_{INPs} values ranged from 10^{-2} to 2 L^{-1} at −25°C and decreased to $<10^{-1}L^{-1}$ at −20°C. At temperatures between −20 and −10°C, n_{INPs} values between $<10^{-2}$ and $<10^{-1}L^{-1}$ were measured. INP measurements at temperatures greater than −10°C were not possible due to the measurement detection limit. The values reported here at temperatures warmer than −15°C likely represent an upper limit of n_{INPs} for this temperature range.

The n_{INPs} results show that at temperatures lower than −10°C, n_{ice} of $<10^{-1}L^{-1}$ may be explained by primary nucleation. In this temperature region, 10-s average n_{ice} values below $10^{-1}L^{-1}$ were observed 65% of times. These also include periods where n_{ice} was below the detection limit (i.e., periods defined only as supercooled). However, it should be noted that the n_{INPs} represents an average over a larger region. Therefore, in Figure S4 in Supporting Information S1 is shown the comparison between n_{INPs} and cloud segment average n_{ice}. It can be seen that in 22

segments where ice was present, the n_{ice} can be explained with primary nucleation, whereas in 21 segments n_{ice} above n_{INPs} were measured. At higher temperatures ($T > -10$°C) n_{INPs} were below the detection limits. If we assume n_{INPs} decrease log-linearly with increasing temperature, similar to previous ship-based measurements in this region (McCluskey et al., 2018), n_{INPs} had likely maximum values of 10^{-3}L^{-1} for temperatures greater than −10°C, indicating extremely low numbers of ice crystals can form via primary ice nucleation in warmer SO mixed-phase clouds. In 50% of times, the 10-s average n_{ice} values were higher than this and n_{ice} exceeded n_{INPs} by three or more orders of magnitude, indicating that SIP is an important process for governing the ice crystal number concentrations in SO mixed-phase clouds.

5. Two Case Studies of Secondary Ice Production

5.1. Rime-Splintering in Generating Cells

Here, we present observations from a single-layer stratocumulus cloud (see Figure S5 in Supporting Information S1 for photograph of cloud top before sampling) associated with the cold ridge of a cyclonic system that was moving through the SO. The stratocumulus layer was sampled in-situ during two ascents and one decent between 3:50 and 4:10 UTC south of Hobart around 58.3°S near the research vessel *Investigator*. Figure 5 shows a time series of meteorological and cloud microphysical parameters. The cloud top was around 1,300 m, observed from the downward (upward) pointing cloud radar when the HIAPER was above (below) cloud during sampling (Figure 5a). Regions of higher reflectivity were observed within the stratocumulus layer, indicating occasional precipitation that was also measured below cloud base (670–830 m). Based on vertical velocities and reflectivity, these precipitating regions were likely embedded with generating cells (Wang et al., 2020). The in-cloud temperature ranged from ∼-4°C at the cloud base to −8°C at the cloud top (Figure 5b), which is well in the rime-splintering range (e.g., Hallett & Mossop, 1974). The maximum cloud water content derived from the CDP was 0.5 g m^{-3} (Figure 5c). The HIAPER was below cloud base, sampling occasional precipitation between 3:52 and 3:54 UTC before the first ascent through the cloud layer that took place between 3:54:30 and 3:55:58 UTC (P1). P1 was outside a region with generating cells. Droplets with $D > 24$ μm were observed in numbers >1 cm^{-3} but no drizzle droplets ($D > 60$ μm) were seen. In the lower part of the cloud (<1 km) 10-s average ice crystal concentrations were 0.2–1.3 L^{-1} and inspection of OAP images revealed that the observed low concentrations were associated with the presence of graupel. Vertical winds were mostly downdrafts (Figure 5g) around −1 m s^{-1}.

The descent between 4:01:22 and 4:02:57 UTC (P2) was through a region with generating cells showing a similar LWC profile (Figure 5c) but in a more updraft dominated region (Figure 5g) compared to P1. RH was observed to be higher than during P1 (Figure 5f), although RH information was occasionally missing. Drizzle droplets were found in maximum concentration of 4.5 L^{-1} and ice crystals were observed throughout the cloud layer with maximum concentrations of up to 205 L^{-1}. Inspection of the ice crystal images (Figure 6) showed the presence of columns and needles. The majority of the crystals were heavily rimed. Some small pristine hollow columns and needles were seen, which can be associated with newly formed crystals (A. Korolev et al., 2020).

The second ascent between 04:06:36 and 04:07:35 UTC (P3) was through another region of generating cells. Again, LWC was similar to P1 and P2 (Figure 5c) and drizzle droplets were present (3 L^{-1}), though not as many as in P2 (Figure 5d). Maximum n_{ice} were 28 L^{-1} (Figure 5e). Ice crystals were observed in the first half in the updraft dominated region whereas in the downdraft region in the second half almost no ice was seen. Observed ice particles were mostly needles.

Between −4 and −8°C, n_{INPs} measured during SOCRATES were below detectable limits ($n_{INP} < 10^{-3}$ L^{-1}, Figure 4) and thus the high n_{ice} in this case study cannot be explained by primary nucleation and were likely a result of SIP. The necessary criteria for rime-splintering are fulfilled: cloud temperatures between −2 and −8°C, and the presence of both large ($D > 24$ μm) liquid droplets and large ($D > 300$ μm) ice crystals acting as rimers (e.g., Hallett & Mossop, 1974; Mossop, 1980). Furthermore, the appearance of (small) columnar crystals in both P2 and P3 are associated with the presence of drizzle droplets, whereas in P1 only graupel without drizzle was observed. Previous studies in SO cumulus clouds have suggested that drizzle size droplets might favor faster splinter production rate (Mossop, 1985).

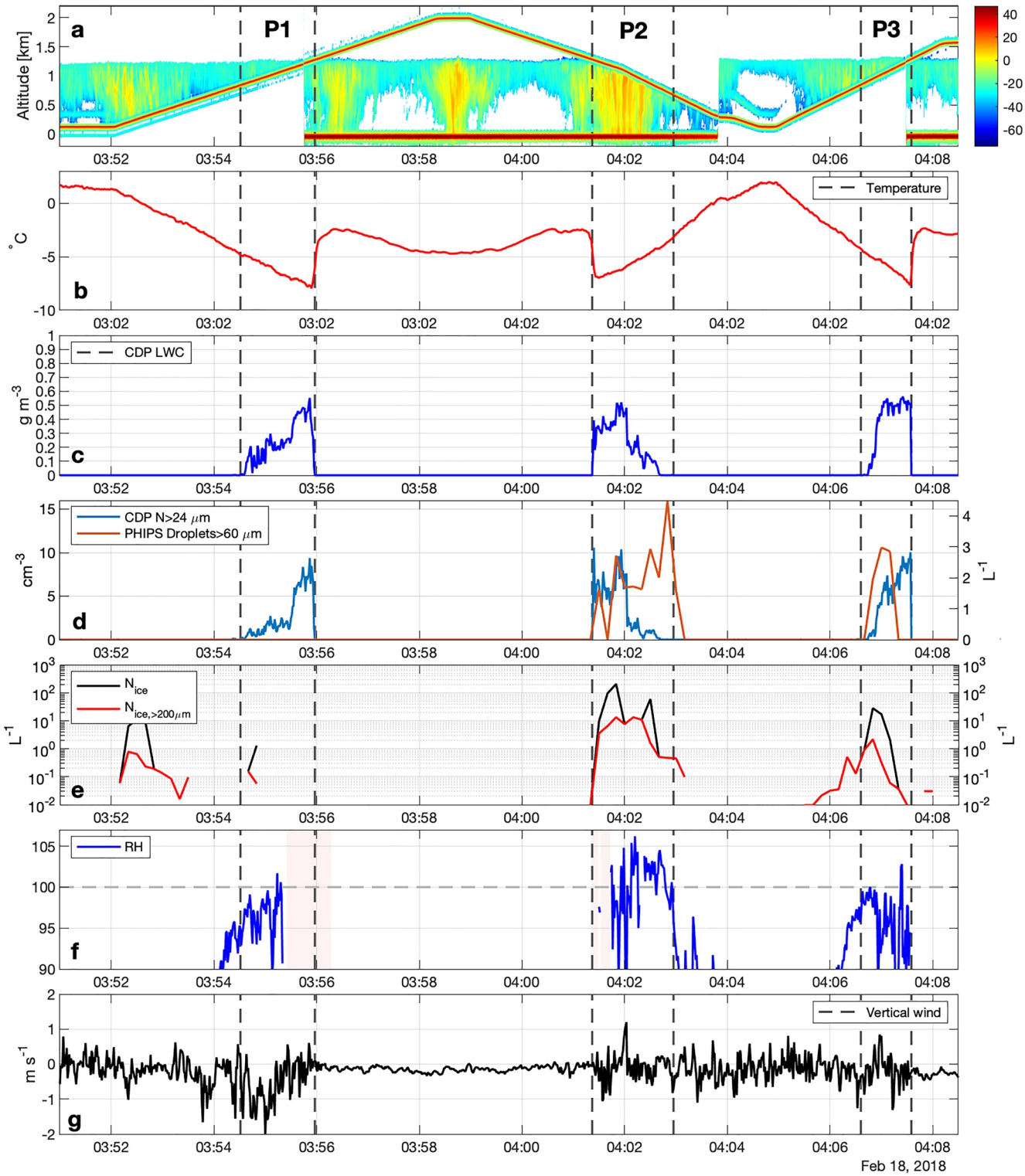

Figure 5. Sampling of a single-layer stratocumulus cloud between 3:51 and 4:08 UTC during RF12. The different panels are as follows: radar reflectivity from the HIAPER cloud radar (panel a), 1-Hz temperature (b), 1-Hz LWC calculated from the CDP (panel c), 1-Hz concentration of droplets with diameters >24 μm (blue) calculated from the CDP and 10 s average concentration of drizzle droplets >60 μm (orange) calculated from the PHIPS (panel d), 10 s average total ice particle number concentration (N_{ice}) (black) and 10 s average ice particle number concentration from 2D-S ($N_{ice,>200\mu m}$) (red) (panel e), 1-Hz relative humidity with respect to water (RH) (panel f), and 1-Hz vertical wind (panel g). Note that RH information was not available between 3:55:20 and 3:55:58 UTC (marked with red shaded area). The cloud passes through regions with CWC >0.001 g m^{-3} are marked with vertical dashed lines and labeled as P1, P2, and P3.

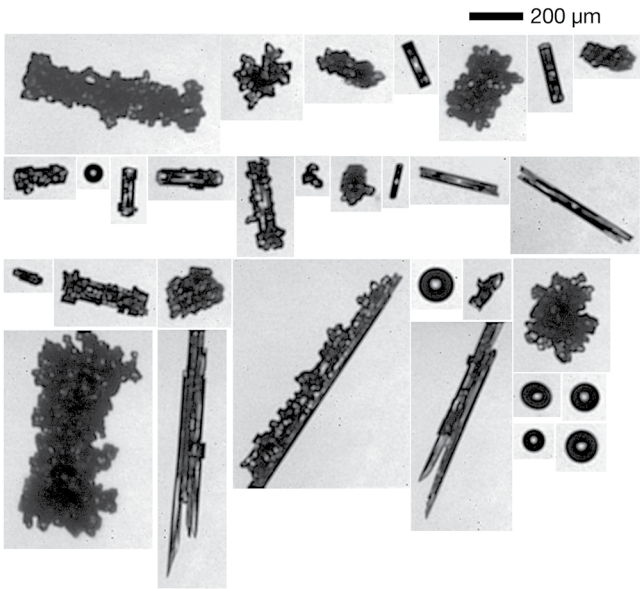

Figure 6. Examples of ice crystals imaged with the PHIPS probe during descent through a generating cell between 4:01:22 and 4:02:57 UTC. Images were taken with the camera assembly 1 (C1) using a 6x magnification.

5.2. Secondary Ice Production at −17°C

During RF09 an extensive stratocumulus deck behind a low-pressure system near Macquarie Island was sampled. The sampled cloud system was one of the coldest low-level cloud cases observed during SOCRATES, with in-cloud temperatures typically less than −8°C. Around 4:11 UTC the broken edge of the system (see Figure S6 in Supporting Information S1 for photograph of cloud top before sampling) around 55.2°S near Macquarie Island was sampled in-situ at a constant altitude of 2165 m.

Figure 7 shows a time series of meteorological and cloud microphysical parameters during a 4 minute sampling period. Radar reflectivity (Figure 7a) shows an area with high reflectivity that was associated with precipitation between 4:13 and 4:14 UTC. Inside this area, LWC was mostly zero and the cloud was completely composed of ice crystals with maximum concentrations of 28 L^{-1} (Figure 7e). Ice crystal images between 4:12:43 and 4:13:59 UTC (Figures 8 and 9) showed both heavily rimed crystals with plate-like growth (crystals 106, 117, 136, and 140) and dendrites (crystals 122, 164, 224, and 230). Outside the area of high reflectivity, LWC was variable with a maximum value of 1.4 $g\,m^{-3}$ and ice crystal concentrations were mostly <2 L^{-1}. Vertical winds were mostly downdrafts (Figure 7g) and the temperature was between −16 and −18°C (Figure 7b). Drizzle droplets were observed only occasionally (Figure 7d).

INPs were sampled below the cloud base before and after sampling the stratocumulus deck. Analysis of the samples showed n_{INPs} concentrations of 0.011 L^{-1} at −21°C, whereas three order of magnitude higher n_{ice} was measured in the precipitation zone. Seeding of ice crystals from aloft layers was not seen from onboard camera imaginary before or after sampling (Figure S6 in Supporting Information S1) although seeding from invisible cloud layers cannot be excluded. The high n_{ice} was likely due to SIP. A probable SIP mechanism in temperatures colder than −8°C is fragmentation of ice crystals in ice-ice collisions (e.g., Takahashi, 1993; Takahashi et al., 1995; Vardiman, 1978). Takahashi (1993) argued that secondary ice can be formed in the collision of large and small graupel (or rimed snow crystals) in weak updraft conditions with low LWC. These conditions were met in this case study. Takahashi et al. (1995) wrote that the surface of small graupel particles should be 'brittle' so that the collision can lead to breaking of branches from the small graupel. The PHIPS images (Figure 8) showed plate-like growth on the surface of the graupel particles (e.g., crystal 140), which might be easily broken in a collision.

On the other hand, it is unclear if ice-ice collisions alone can explain the observed n_{ice}. The low n_{INPs} (0.011 L^{-1}) would lead to a low number of primary ice that might not get to a point of collision. Figure 8 also showed that riming of the ice crystals was common, which could also indicate that SIP could have also occurred or initiated through riming. However, the exact mechanism for rime-splintering at temperatures below −8°C is unknown.

6. Possible SIP Mechanisms in SO Stratocumulus Clouds

In this section we explore the known SIP mechanisms that could be behind the high n_{ice} exceeding the number of INPs in the SO summer-time stratocumulus clouds.

6.1. Rime-Splintering and HM Process

Previous airborne studies in the SO region (see Table 1) and other airborne studies have observed high n_{ice} in relatively warm (−2 to −8°C) maritime cumulus clouds (e.g., Lasher-Trapp et al., 2016) that have been explained by ice multiplication caused by rime-splintering. Similarly, our observations show a maximum in n_{ice} in the same temperature region (Figure 4), where rime-splintering and HM process are active.

From the 385 stratocumulus profiles, 191 were conducted in the HM temperature range. In 122 (out of 191) cases, n_{ice} above the detection limit was detected. Figure 10 shows relative frequency histograms of environmental conditions observed for cases with (*HMobs with ice*) and without ice observations (*HMobs w/o ice*). It

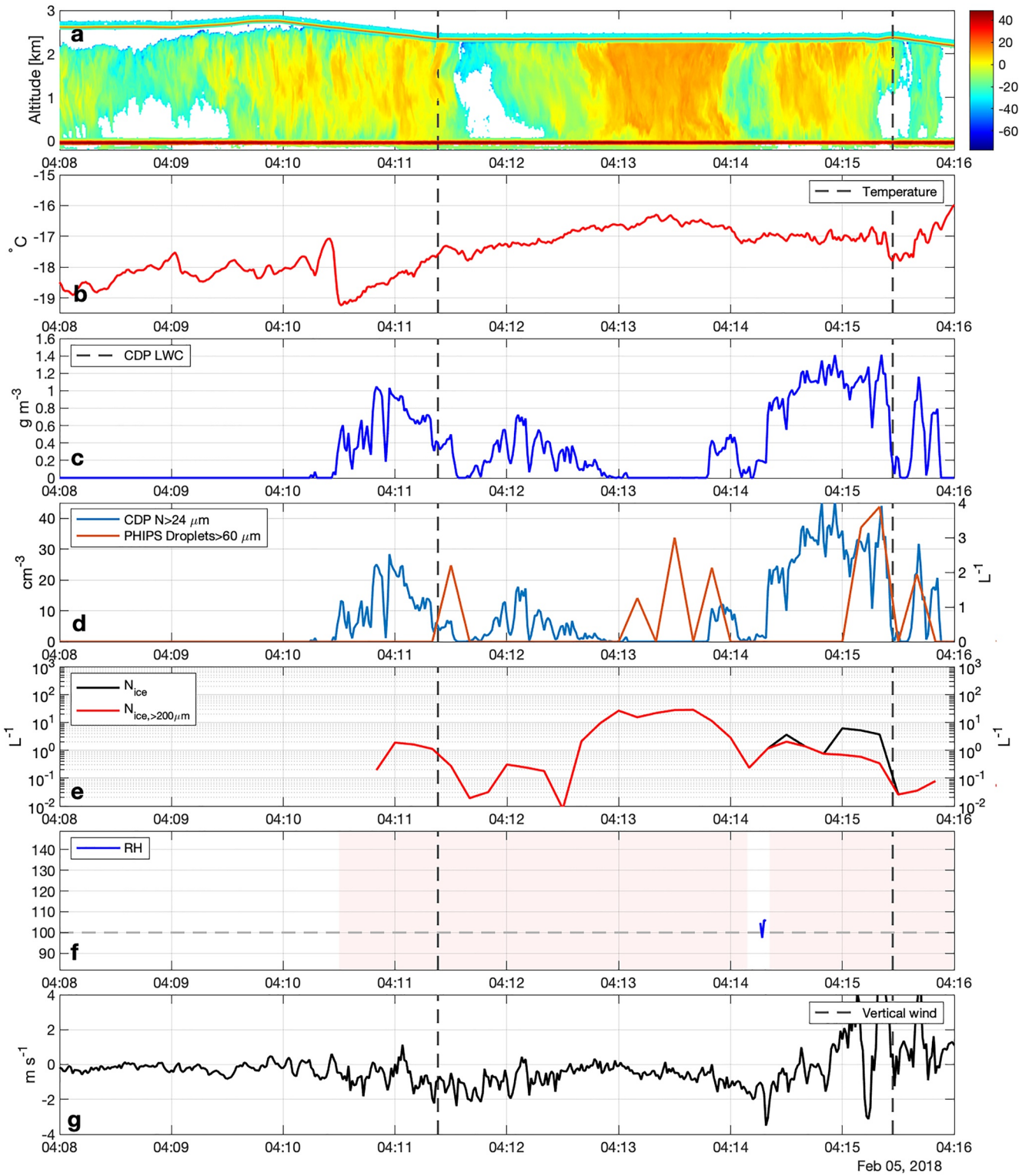

Figure 7. Same as Figure 5 but fa segment through stratocumulus cloud between 4:11:23 and 4:15:27 UTC during RF09. Note that relative humidity information was not available for most of the period (shown as red shaded area in panel f), as the VCSEL hygrometer was constantly switching modes in this time period and the data had to be removed.

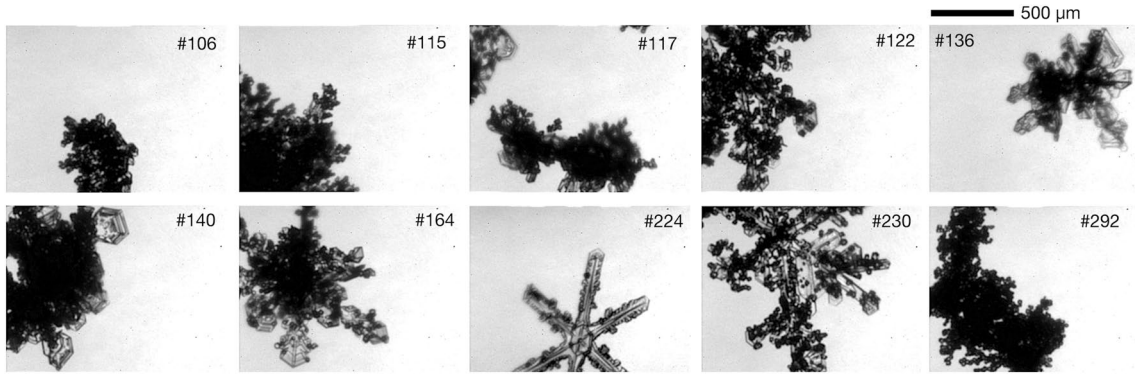

Figure 8. Examples of PHIPS images of ice crystals taken between 4:12:43 and 4:13:59 UTC during RF09. Images were taken with the camera assembly 1 (C1) using a 6× magnification. Each frame has a width of 1.33 mm.

can be seen that cases with observed ice are associated with higher LWC, higher concentration of cloud droplets larger than 24 µm, larger threshold diameter (D_t, defined as the droplet diameter for which total concentration of droplets with greater diameter is 3 cm^{-3}, Rangno and Hobbs (1991)) and higher drizzle droplet concentrations. Unlike previous airborne studies (Hobbs & Rangno, 1985; Rangno & Hobbs, 2005), we did not find a correlation between observed ice crystal concentrations and number of cloud droplets $D > 24$ µm or D_t (Table 2). However, it should be noted that the stratocumulus clouds were sampled only once and, therefore, the observed cases represent different development stages of the clouds. Hence, in some of the *HMobs with ice* cases most or all of the LWC may have been depleted through the Bergeron-Findeisen process and through riming.

Rime-splintering is supported by the fact that all of the 122 *HMobs cases with ice* also had ice crystals with $D_e > 200$ µm present. Inspection of PHIPS ice crystal stereo-images revealed that most of these crystals were rimed. The splinter production rate in the *HMobs cases with ice* was estimated following the approach of Willis and Hallett (1991) (see Appendix B). One splinter production rate was calculated for each of the cloud segments. Figure 11 shows the estimated splinter production rate as a function of the measured ice concentration for stratocumulus cases (blue dots) and for cumulus cases (red dots). The estimated splinter production rate follows a relationship of $dN/dt = 5 \times 10^{-6}N$. At this rate, it would take 200 hr to increase ice crystal concentration from 1 L^{-1}–100 L^{-1}, which is not a feasible multiplication rate considering the lifetime of SO stratocumulus clouds. Mossop (1985) estimated a faster rate of $dN/dt = 1.7 \times 10^{-3}N$ in winter-time cumuli near Tasmania.

It is a common finding that the rime-splintering mechanism (as presently formulated) cannot explain the ice crystal production rate in some clouds (Hobbs & Rangno, 1990; A. Korolev et al., 2020; Rangno & Hobbs, 1991). It has been suggested that large droplets might enhance the ice multiplication rate by forming large crystals upon freezing that can immediately act as rimers (Mossop, 1985). The presence of large drops have been found to favor ice multiplication (Braham Jr, 1964; Koenig, 1963; Mossop, 1978; Mossop et al., 1968). Our results support the idea that large droplets might be important for ice multiplication at temperatures above −8°C, however, the exact role of large droplets for enhancing rime-splintering remains unclear.

Another factor potentially enhancing production of ice in the stratocumulus clouds is related to the multi-cell structure of the clouds (see Section 5.1) (Lasher-Trapp et al., 2021; Mossop et al., 1970). Ice crystals from older cells can be incorporated into newly forming rising cells, where they can initiate ice multiplication processes. Section 5.1 showed how first ice crystals were found to be graupel particles that could potentially originate from generating cells or from freezing of large drizzle droplets. These can act as rimers and produce splinters that grow into columnar particles. In a later phase of the multiplication process, the cloud is dominated by columns and needles, some of them acting as new rimers.

6.2. Ice-Ice Collisions

Laboratory studies have shown that ice-ice collisions produce a maximum ice ejection rate at −16°C (Takahashi et al., 1995). Requisite is that the colliding ice particles have different surface properties (e.g., small graupel with 'brittle' surface and large graupel with 'compact' surface). Figure 4 showed an increase in the observed n_{ice}

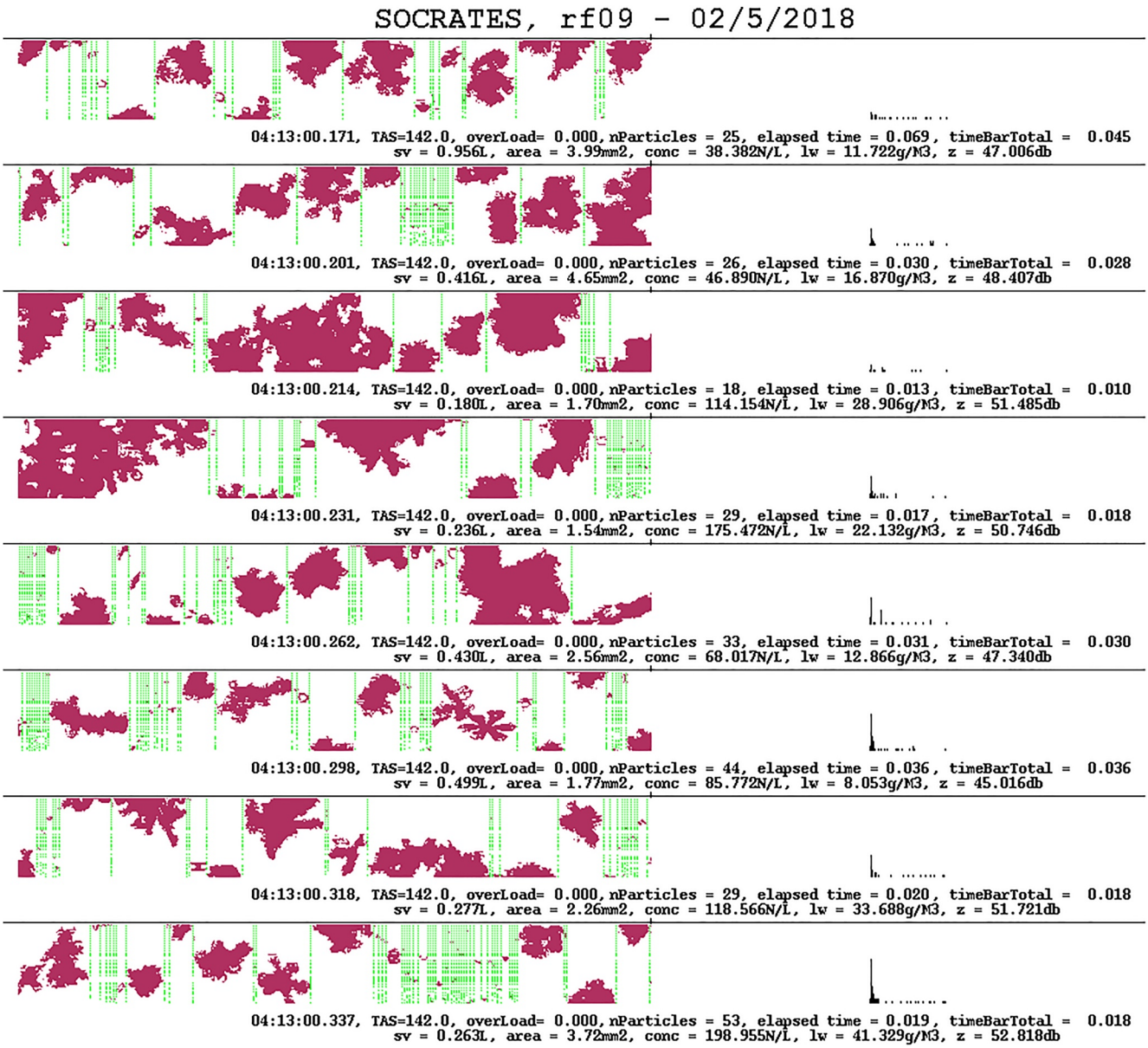

Figure 9. Examples of 2DC shadowgraphs taken at 4:13:00 UTC in the region of high reflectivity. Shadowgraphs show simultaneous existence of compact irregular particles that closely resemble crystals 106, 115, 140, and 292 in Figure 8 and dendrites that correspond to crystals 224 and 230 in Figure 8.

between −14 and −19°C that corresponds to the temperature of maximum ice ejection rate found in laboratory work. Ice-ice collisions as a possible SIP mechanism in the colder temperatures is also supported by the fact that in all cases where ice concentration above 1 L^{-1} were observed, dendrites or compact ice crystals with plate-like branches were observed, as seen in Section 5.2. These observed ice branches may contribute to ice particle ejection in collisions.

Since the physical mechanism behind ice-ice collision is still largely unknown, it is difficult to estimate if this process alone could explain the observed ice concentrations in the temperature range below −8°C. Also, the large gap between n_{INP} and n_{ice} would likely hinder ice-ice collisions. It cannot be excluded that other SIP mechanisms would play a role in the T < −10°C range.

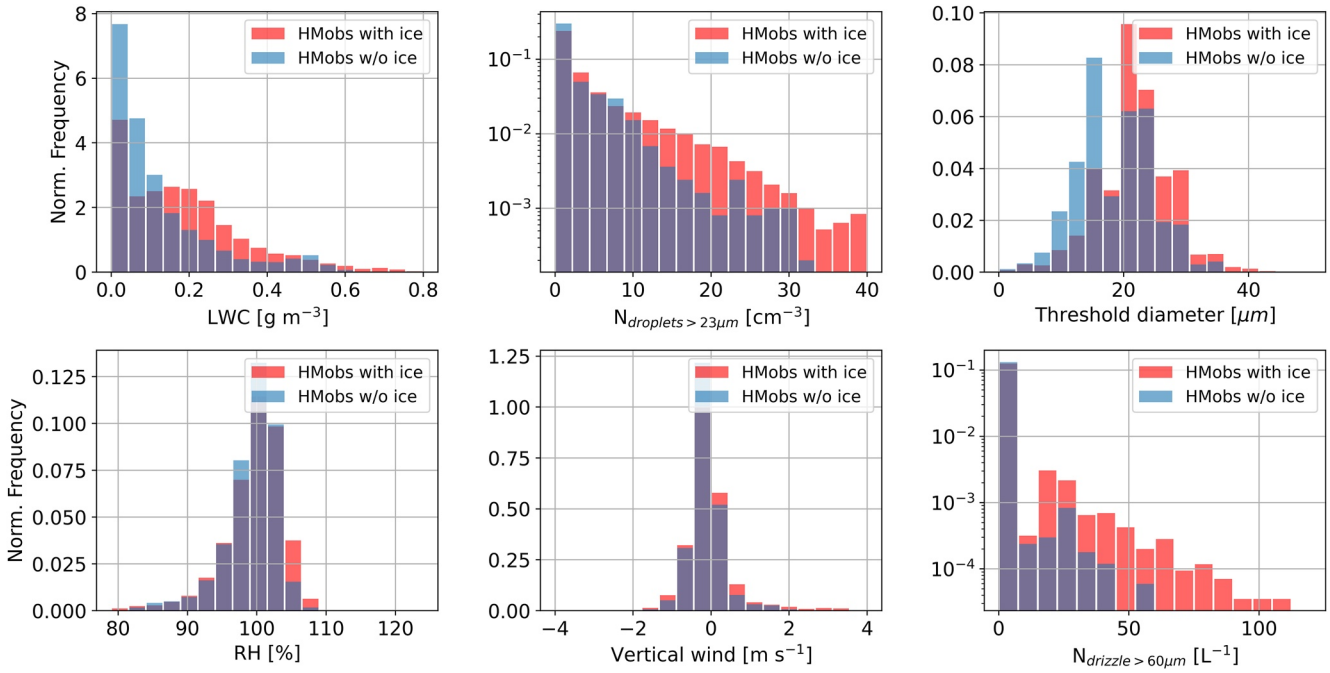

Figure 10. Relative frequency histogram of 1-Hz LWC values, 1-Hz concentration of cloud droplets larger than 24 μm, 1-Hz threshold diameter, 1-Hz relative humidity (RH) with respect to water, 1-Hz vertical wind speed and 1-Hz average concentration of drizzle (>60 μm) droplets for the cloud segments in the HM temperature range where ice was observed (red bars, $N = 122$) and where ice concentration was below the detection limit (blue bars, $N = 69$). Purple color illustrates the overlap area of the two cases. *p*-values for all the observation pairs are below 0.05. Values are normalized so that the area under the histogram integrates to 1.

6.3. Droplet Fragmentation During Freezing

A SIP mechanism that has gained a lot of attention recently is the fragmentation of large drizzle-sized droplets during the freezing process (e.g., A. V. Korolev et al., 2004; A. Korolev et al., 2020; R. P. Lawson et al., 2015; P. Lawson et al., 2017; Rangno, 2008). Recent laboratory work has shown that when droplets freeze, they develop a frozen shell whilst the inside remains liquid, generating outward pressure on the ice shell. In some cases, the ice shell can break, causing splitting of the droplet or ejection of small ice particles (Lauber et al., 2018). Some droplets produce a visible "spicule", which has led to a search for frozen spicule droplets in natural clouds.

Droplet fragmentation is most active in clouds colder than −10°C where large drizzle droplets are present (Lauber et al., 2018). From the 104 profiles in the < −10°C temperature range, 31 showed drizzle droplets and 26 profiles had both drizzle and ice present. However, no clear correlation between drizzle droplet and ice crystal concentrations was found (Table 2).

Table 2
Correlation Coefficients (R) Between Number Concentrations of All Ice (N_{ice}) or Small Ice ($N_{ice<100}$) Crystals and Vertical Wind (w), Liquid Water Content (LWC), Concentration of Droplets >23 μm ($N_{drops>23\mu m}$), Threshold Diameter (D_t) and Concentration of Drizzle Droplets >60 μm ($N_{drizzle}$) With 10 s Averaging and for Different Temperature Ranges

	w	*LWC*	$N_{drops>23\mu m}$	D_t	$N_{drizzle}$
N_{ice} (complete T range)	−0.04	0.004*	0.07*	0.07	0.08
N_{ice} (−2.5 to −8°C)	−0.04*	0.02*	0.06*	0.11	0.13
N_{ice} (−14 to −19°C)	−0.009*	−0.06*	0.0005*	0.12	0.17
$N_{ice<100\ \mu m}$ (complete T range)	−0.04*	−0.007*	0.03*	0.07	0.06
$N_{ice<100\ \mu m}$ (−2.5 to −8°C)	−0.05*	0.02*	0.06*	0.11	0.12
$N_{ice<100\ \mu m}$ (−14 to −19°C)	0.46	0.70	0.75	0.37	0.53

Note. Correlation coefficients with p-value > 0.05 are not statistically significant and are marked with an asterisk.

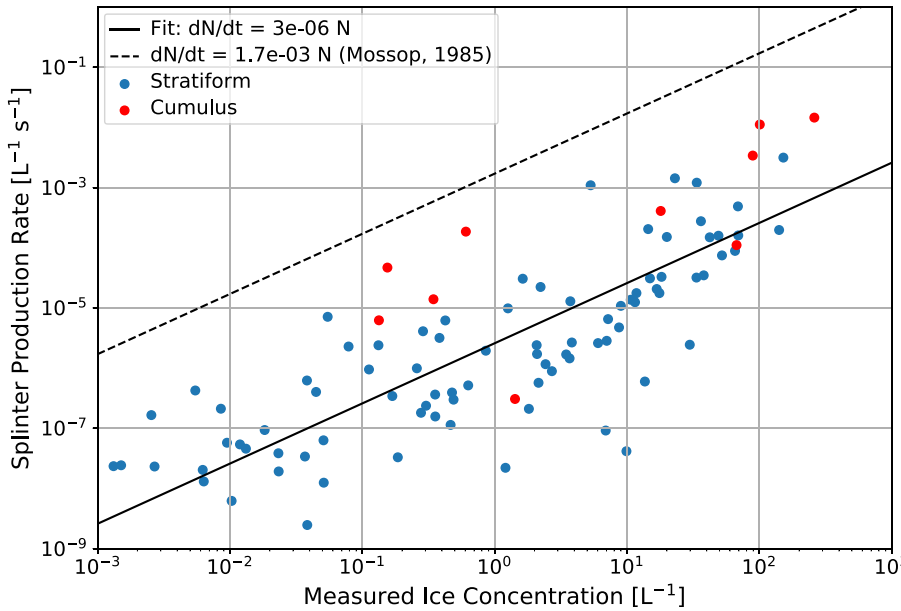

Figure 11. Predicted splinter production rate as a function of measured ice particle concentrations for cloud segments that were found to be in the HM temperature rage (see Table S1 in Supporting Information S1). Cloud passes in stratiform clouds are marked as blue and passes in cumulus clouds as red. The splinter production rate was estimated following the approach of Willis and Hallett (1991). The solid line represents the fit through the data and the dashed line the relationship that was estimated by Mossop (1985) in small winter-time cumuli near Tasmania.

Evidence for droplet fragmentation was investigated using the cloud particle stereo-microscopic imagery. These showed occasional frozen drizzle droplets that were either single frozen droplets or attached to the surface of larger ice particles (Figure 12). Single frozen droplets were found in the temperature regime of $T > -5$°C, which is warmer than where splinter production is expected (Lauber et al., 2018). The single frozen droplets always had an uneven surface, which could be an indication of fracturing. Direct evidence of splitting was seen on crystal 415. It is possible that these around 150–200 µm frozen droplets were frozen in an upper, colder part of the cloud, where they could have produced splinters and afterward fallen into warmer, lower parts of the cloud.

Frozen drizzle droplets were not observed at colder temperatures with the exception of one cloud segment. This segment showed higher than average ice crystal concentrations, $n_{ice} > 1$ L^{-1}. Stereo-microscopic images showed that large drizzle droplets were frequently collected by larger ice crystals (crystals 4,729–5,032 in Figure 12). These drizzle droplets could have produced splinters in the freezing process, although no clear sign of spicule formation was seen in the images.

Based on the 104 cloud segments that were measured below −10°C it is difficult to estimate whether droplet fragmentation is a significant process in SO stratocumulus clouds as frozen drizzle droplets were only rarely observed in the stereo-microscopic images. However, it should be noted that the statistics of the single particle measurements in cloud segments of a few minutes is not adequate to make conclusions about the significance of the discussed mechanism. Since in the pristine SO environment drizzle-sized droplets are frequently observed, it is possible that droplet fragmentation, even if not the dominant SIP mechanism, could act as an initiator for SIP, as suggested by A. Korolev et al. (2020). Also, previous studies have reported the presence of large drizzle droplets preceding the initiation of glaciation (Rangno & Hobbs, 1991).

6.4. Other SIP Mechanisms

Other proposed mechanisms for SIP include activation of INPs in localized pockets of high-supersaturation areas, fragmentation of ice crystals after collision with supercooled droplets, and fragmentation due to sublimation.

Localized pockets of high-supersaturation areas can be found within the vicinity of a freezing droplet (Dye & Hobbs, 1968; Fukuta & Lee, 1986; Nix & Fukuta, 1974) or during growth of droplets by collision (Rangno &

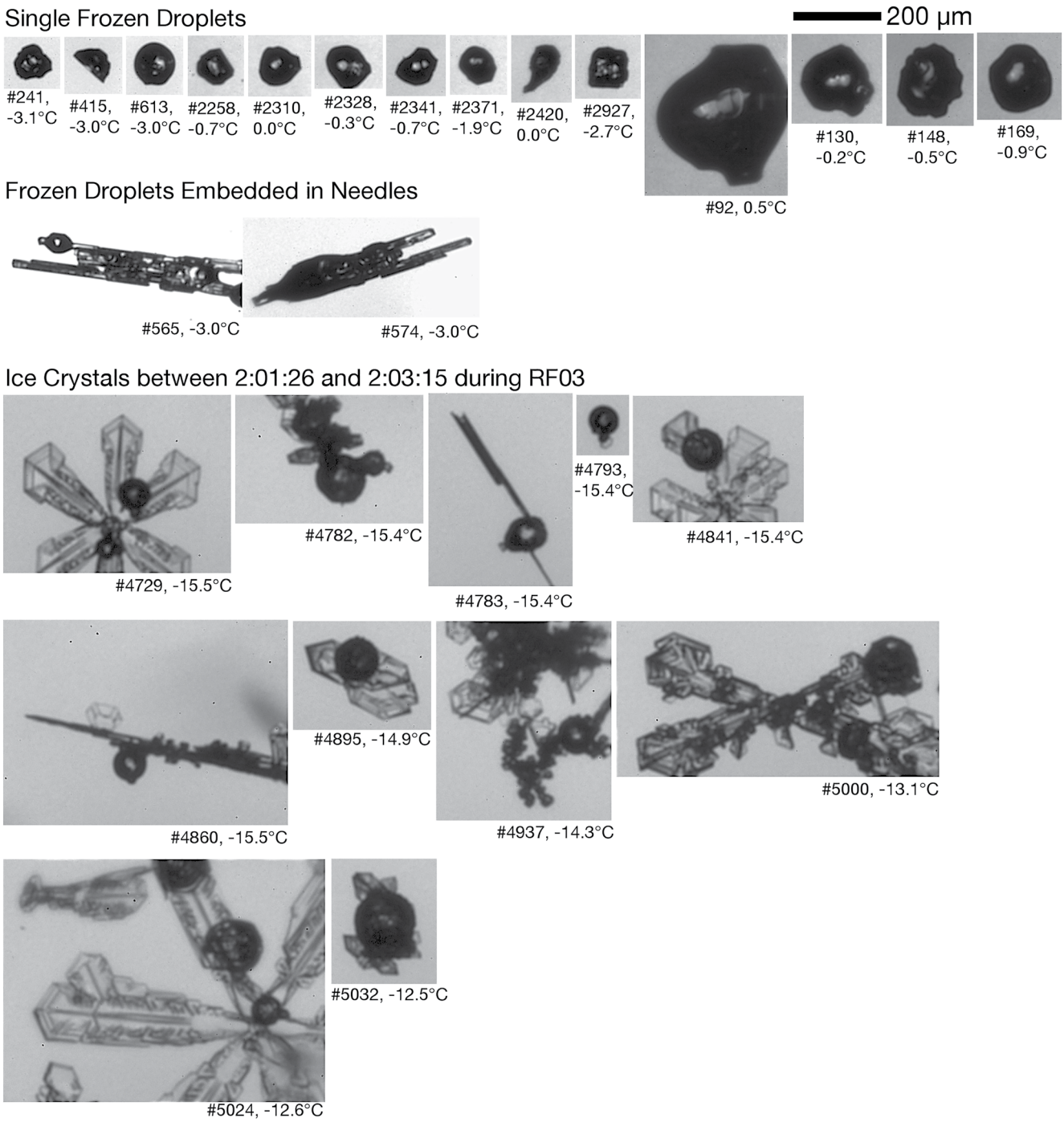

Figure 12. Examples of microscopic images of single frozen droplets, droplets frozen on needles and droplets frozen on crystals at −15°C.

Hobbs, 1991). This process is relevant especially at cold temperatures (<−10°C). At −20°C, supersaturation with respect to water of 15%–20% can be reached during droplet freezing (Dye & Hobbs, 1968; Nix & Fukuta, 1974), which could increase INP concentrations by an order of magnitude (Hussain & Saunders, 1984). This very localized effect would play a role near freezing drizzle droplets or during riming processes. The activation of INPs in high supersaturation regions cannot be excluded, but it probably cannot explain ice concentrations that are more than an order of magnitude higher than INP concentrations.

Some evidence of the riming-related SIP mechanism in the temperature range of −14 and −19°C is given in Table 2 that shows a moderate correlation between the concentration of small ice crystals and LWC ($R = 0.70$) and concentration of cloud droplets with $D > 23$ μm ($R = 0.75$). King and Fletcher (1976) demonstrated that ice crystals can fragment due to the thermal shock caused by droplet freezing on the surface. This mechanism depends on the size of the droplet and the shape and size of the ice crystal. For example, a thin plate rimed with a large droplet would shatter only if the temperature was below −10°C (King & Fletcher, 1976). Stereo-microscopic images of plates rimed with drizzle droplets (Figure 12) did not show evidence of shattering (only shattering in the instrument inlet was seen in the case of particle 5024) but based on the observation we cannot confirm or deny that this mechanism would play a role.

Ice crystals can also fragment due to sublimation. This process can be active only in clouds completely composed of ice in ice sub-saturated conditions. In our study, most of the ice crystals were observed together with liquid water and no sign of sublimation was detected in the stereo-microscopic images.

6.5. Seeding

Higher level clouds above the sampling altitude were identified using HIAPER cloud radar and onboard cameras. In 150 (out of 327) cloud segments clouds above the sampling level were found. Seeding of ice crystals from colder clouds above can potentially affect the ice crystal concentrations in the lower clouds (Figure 13). Statistical analysis of cloud cases with clouds observed above the sampling altitude and those without showed higher mean n_{ice} values, although high ($n_{ice} > 50$ L^{-1}) concentrations were observed also for single-layer clouds with no visible higher level clouds (see Figure S7 in Supporting Information S1). Therefore, seeding alone cannot explain the observed ice crystal number concentrations, although it may play a role in the initiation of SIP in multi-layer cloud situations by transporting rimers to the HM temperature range or by enhancing collisional break-up in colder clouds at temperatures below −10°C (Georgakaki et al., 2022). For example, from all the cloud segments where the minimum temperature was observed to be below −10°C, and where clouds above the in-situ sampling were observed (26 segments), 62% had n_{ice} above 0.1 L^{-1}, whereas from those segments without detectable cloud layers above in-situ sampling slightly less, 42%, had n_{ice} above 0.1 L^{-1}.

7. Comparison of Observed and Simulated Ice Crystal Concentrations

Observational evidence presented in this study suggests that multiple SIP processes might be active in SO clouds. However, many global climate models have limited representation of SIP (P. R. Field et al., 2017). In fact, the HM rime splintering process serves as the only SIP process in CAM6, active between −8 and −3°C (Cotton et al., 1986; Section 2.4). Here, we expand the previous assessments of simulated clouds in CAM6 (Gettelman et al., 2020) to consider n_{ice} predicted in nudged simulations from the SOCRATES campaign.

Gettelman et al. (2020) demonstrated that nudging CAM6 to MERRA-2 reanalysis resulted in temperatures within 1–2°C of measured temperatures during all SOCRATES flights, with some issues resolving the boundary layer inversion that likely resulted in high biases in the relative humidity vertical structure. Their results suggest that the CAM6 base nudged simulation represents the general observed meteorological conditions during the SOCRATES flights. Additionally, the simulations successfully generated clouds in the same grid points where they were also observed during RF07 (Gettelman et al., 2020). We follow their approach by sampling CAM6 data along the flight tracks for RF02-RF15, resulting in representative temperature and altitude distributions (see Figure 3). The mean simulated temperature distributions were 0.7°C colder compared to observations and the mean cloud altitudes were 130 m lower in model than in observations. Furthermore, higher occurrences of RH greater than 100% were seen in the observations compared to the model.

While Gettelman et al. (2020) found similar amounts of liquid water content compared to SOCRATES observations, simulated IWC was biased low compared to SOCRATES observations. We also note that the IWC observations were also associated with high uncertainty and variability. Here, we evaluate simulated n_{ice} using instrument simulators that include instrument-specific size ranges and detection limits. Simulated gamma distribution parameters for ice and snow hydrometeors were used to reconstruct number size distributions. These number size distributions were integrated to determine the number concentration of ice particles (ice and snow) with diameters of 30–200 μm and 200–3,000 μm for the PHIPS (n_{PHIPS}) and 2DS (n_{2DS}), respectively. Given the size range for simulated ice and snow particles, simulated n_{PHIPS} will include more model ice whereas simulated

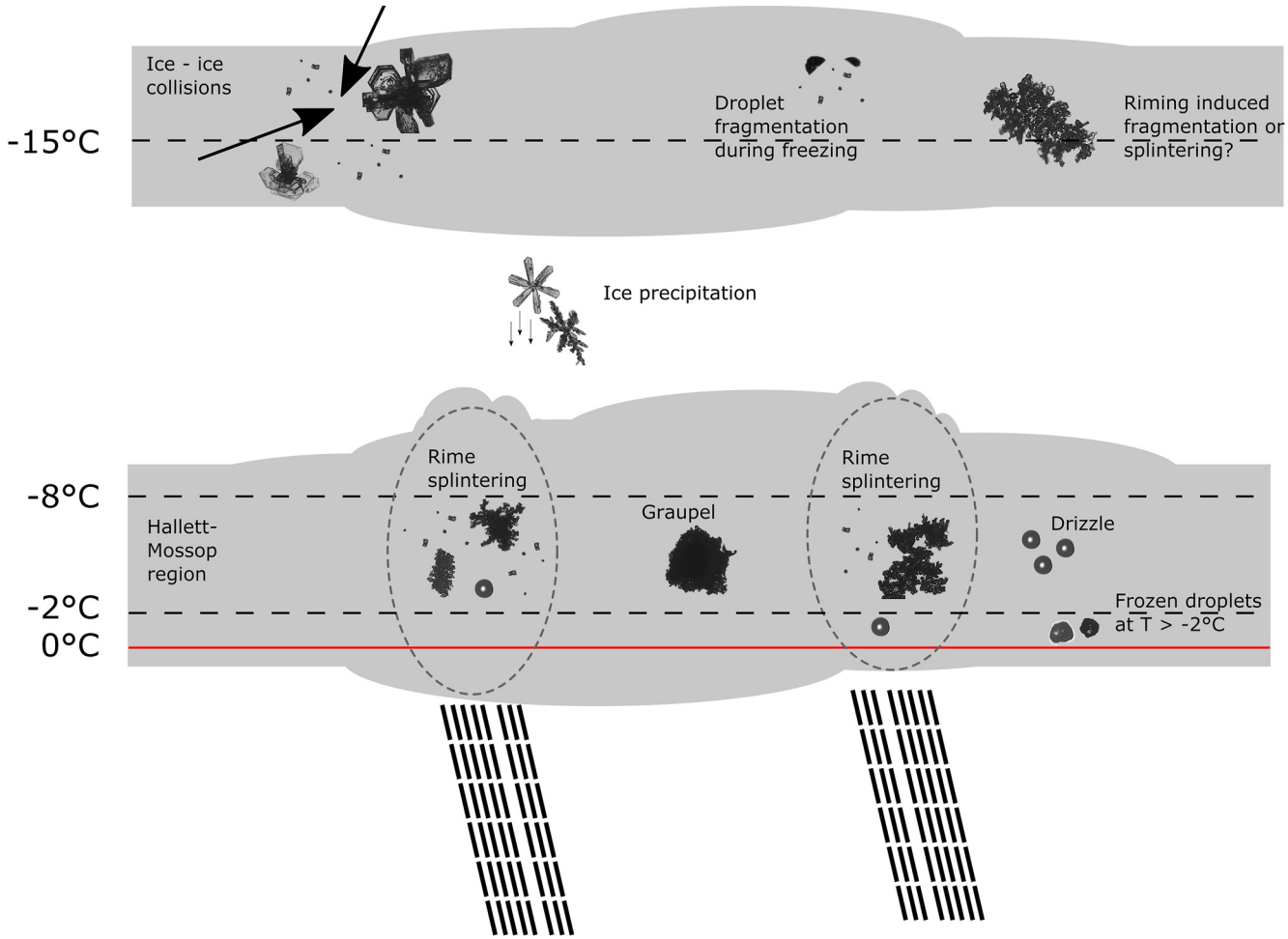

Figure 13. A schematic illustration of SIP observed in the SO stratocumulus clouds. At temperatures greater than −10°C indication for rime splintering was seen in regions with generating cells. Outside these regions occasional graupel particles were detected. At temperatures below −10°C potential SIP include ice-ice collisions involving dendrites or ice crystals with plate-like growth, and droplet fragmentation during freezing. Rimed crystals were frequently observed at $T < -10$°C. Many of the observed cloud systems were multilayered, which could promote seeding from higher cloud layers to lower clouds. Sometimes frozen drizzle droplets were also found at temperatures greater than −2°C.

n_{2DS} will include more model snow. Detection limits, or lower limits, of 3 L^{-1} and 0.008 L^{-1} were also applied to simulated n_{PHIPS} and n_{2DS}, respectively. Simulated n_{PHIPS} and n_{2DS} were estimated along the flight track and were averaged over the same 10-s averaging period used for the measurements. We statistically compared 10-s average observed and simulated n_{2DS} (Figure 14) and n_{PHIPS} (Figure 15) in 2°C temperature bins between −20 and 0°C.

We first assess default (base) simulated and observed ice particles between 200 and −3,000 µm (n_{2DS}) greater than 0.008 L^{-1} for cloud temperatures between −20 and 0°C (Figure 14). According to the observations, 35%–85% of the 10-s periods in clouds contained detectable ice, with only 68% of the clouds containing detectable ice between −20 and −22°C. Simulated clouds at temperatures warmer than −8°C had similar cloud ice fractions to observed clouds (with the exception of the temperature bin from −2 to −4°C); whereas clouds at temperatures colder than −8°C contained more ice with over 90% of simulated clouds containing ice between −14 and −22°C (Figure 14a). While the frequency of ice occurrence in simulated clouds was similar for warmer temperatures, median simulated n_{2DS} were frequently statistically different compared to the observations. For temperatures between −8 and 0°C, median simulated n_{2DS} were mostly within the interquartile range of observed n_{2DS}, whereas median simulated n_{2DS} were lower than observed n_{2DS} up to a factor of 10 for temperatures warmer than −6°C. Below the HM temperature range (below −8°C), the interquartile range of simulated n_{2DS} at some temperatures exceeded observed n_{2DS} and at other temperatures were within the interquartile range of observed n_{2DS}.

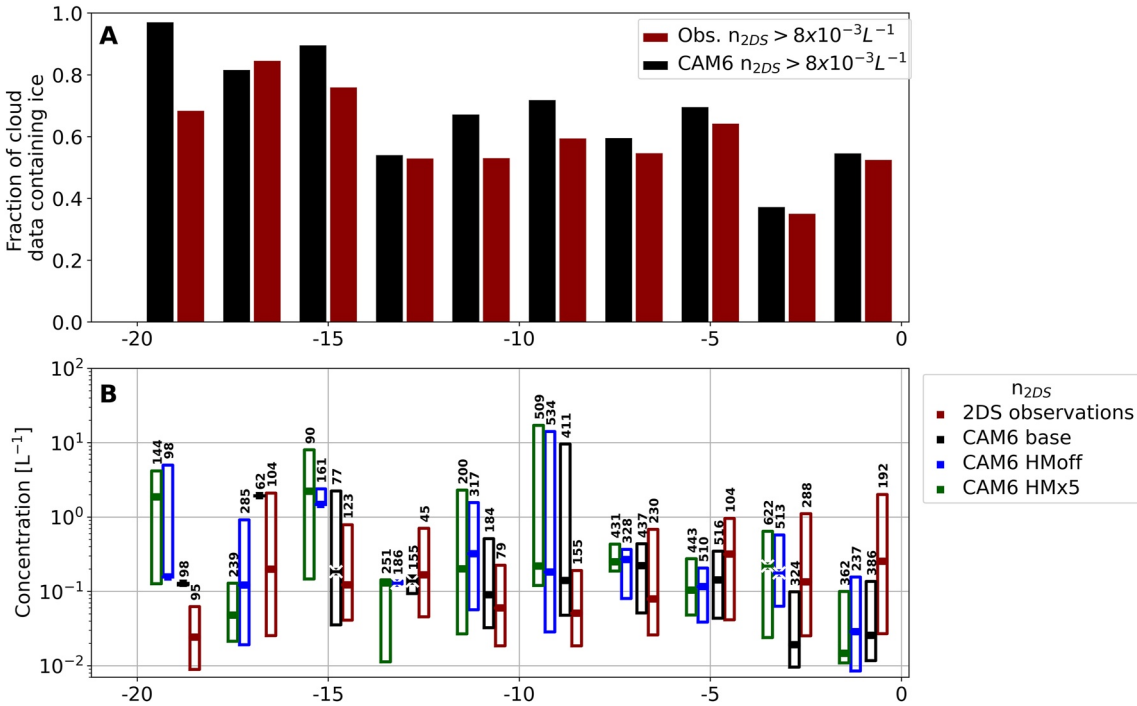

Figure 14. Statistical analysis of observed and simulated number concentrations of ice particles within the 2DS size range (n_{2DS}, 200–3,000 μm). Observations (red) are 10-s averaged n_{2DS} measured by the 2DS probe. Model n_{2DS} were estimated from three simulations to match the 2DS size range and observation averaging period. Additionally, simulated n_{2DS} below the 2DS instrument detection limit (0.008 L^{-1}) were excluded. All data were binned in 2°C temperature bins. Panel A shows the fraction of 10-s averaged observed (red) and simulated (base simulation, black) points within each temperature bin with detectable n_{2DS}. In panel B, median and interquartile ranges for observed n_{2DS} were calculated using 10-s average observed n_{2DS} (dark red symbols). Simulated median and interquartile ranges were also calculated from 10-s averaged simulated n_{2DS} from three simulations: CAM6 base simulation (black), CAM6 with HM ice multiplication rate set to 0 (blue) and CAM6 with HM ice multiplication rate enhanced by a factor of 5 (green). For simulated n_{2DS}, median markers with white crosses indicate distributions of n_{2DS} that are statistically insignificantly different ($p > 0.05$) from n_{2DS} simulated in the CAM6 base simulation according to the Mann-Whitney U test. The number above the boxes shows the number of data points included into the statistical analysis.

The same analysis as above was performed for small ice particles, those between 30 and −200 μm corresponding to measurements by the PHIPS (n_{PHIPS}). The PHIPS detection limit (3 L^{-1}) is higher than the 2DS, meaning the PHIPS targets high concentrations of small particles, or conditions indicative of HM rime splintering. As such, the fraction of clouds containing n_{PHIPS} greater than 3 L^{-1} (Figure 15a) ranged from less than 10%–23%, significantly lower than the fraction of clouds containing n_{2DS} greater than 0.008 L^{-1} (Figure 14a). Observed clouds containing measurable high n_{PHIPS} were more common at temperatures warmer than −8°C indicative of an active HM process in observed clouds. Simulated clouds at temperatures warmer than −8°C with n_{PHIPS} greater than 3 L^{-1} were less common than observed frequencies, with less than 8% of clouds with detectable ice compared to observed 12%–23%. While the frequency of occurrence of ice was lower in simulated clouds (CAM6 base), simulated n_{PHIPS} were within the observed interquartile range of n_{PHIPS} for temperatures above −8°C and the median simulated n_{PHIPS} were even statistically not significantly different to observations at temperatures above −4°C (Figure 15b). At temperatures lower than −8°C, simulated clouds frequently (up to 80% of cloud data) contained n_{PHIPS} greater than 3 L^{-1}. Between −10 and −8°C, the interquartile range of simulated n_{PHIPS} exceeded the 75th percentile of observed n_{PHIPS}, indicating simulated clouds too frequently contained ice and had too high n_{PHIPS} at temperatures between −10 and −8°C. For temperatures below −10°C comparison of the simulated and observed ice concentrations was not possible due to removal of observational data caused by shattering artifacts.

To investigate the sensitivity of the model to the HM process, we evaluated ice concentrations simulated in two sensitivity simulations presented in Gettelman et al. (2020) that modified the HM parameterization. The *HMoff* simulation reduced the HM ice multiplication rate to 0 across all temperatures and the *HMx*5 simulation increased the multiplication rate by a factor of 5. If the modeled HM process controls ice concentrations between −8 and −3°C, the simulated n_{2DS} and n_{PHIPS} should significantly decrease (increase) with the HM process turned off (increased by a factor of 5). However, the results of the sensitivity tests indicate that the model HM process

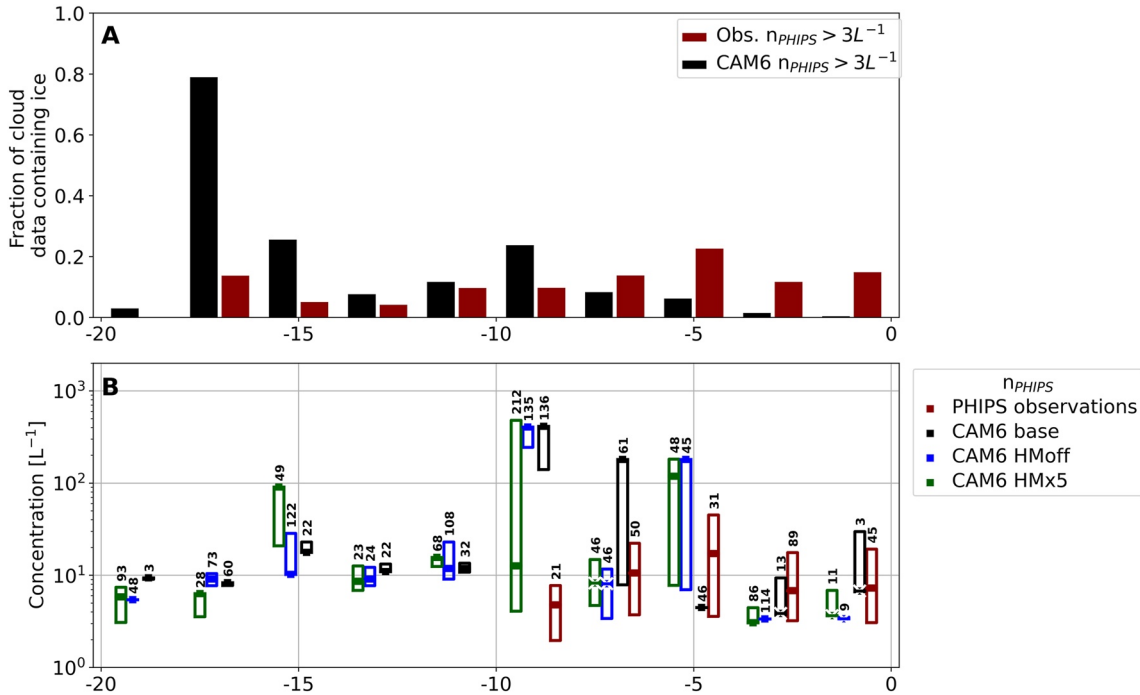

Figure 15. Same as Figure 14 but for ice crystals within the PHIPS size range (n_{PHIPS}, 30–200 μm). Observations are 10-s averages from the PHIPS probe. Model n_{PHIPS} were estimated from three simulations to match the PHIPS size range and observation averaging period. Additionally, simulated n_{PHIPS} below the PHIPS instrument detection limit (3.0 L^{-1}) were excluded. In panel B statistical analysis is only shown if more than 10 data points were available.

did not significantly influence simulated n_{2DS} or n_{PHIPS} in the HM temperature range. For the larger size range (200–3000 μm) with lower detection limit (n_{2DS}, Figure 14b), simulated clouds in the HM temperature range actually contained higher concentrations when the HM process was turned off (HMoff) compared to the base simulation. For simulated clouds with enhanced HM ice multiplication rate (HMx5), simulated n_{2DS} were only statistically significantly higher compared to the base simulation for temperatures between −4 and −2°C and −8 and −6°C. For the smaller size range (30–200 μm) with higher detection limit (n_{PHIPS}, Figure 15b), simulated clouds without an active HM process (HMoff) contained n_{PHIPS} that were statistically lower than base simulated n_{PHIPS} for temperatures between −4 and −2°C. For temperatures between −6 and −4°C the simulated clouds without HM process showed statistically higher concentrations compared to the base case. Simulated clouds with an enhanced HM process (HMx5) contained n_{PHIPS} that were statistically significantly lower by a factor of 1.3 and 1.5 for temperature bins −6 to −4°C and −4 to −2°C, respectively.

These co-located instrument simulator analyses performed for the low-level mixed phase clouds probed during SOCRATES indicate that the CAM6 is skilled in simulating cloud ice frequency when considering larger ice particles, but is deficient in simulating ice number concentrations in most of the temperature regions for both small and large particles. In the HM temperature range the simulated n_{2DS} and n_{PHIPS} were found to be mostly in the interquartile range of the observations. Modifications to the HM process had little influence on simulated n_{2DS} or n_{PHIPS} in the HM regime, suggesting that the HM process in CAM6 is only slightly active in the simulated clouds for SOCRATES, inconsistent with observational evidence of active SIP clouds observed during SOCRATES. The extent to which CAM6 is accurately representing the HM process and all other processes (ice nucleation, sedimentation, etc.) is unclear from these results and requires additional model retooling to assess number tendencies or particle tracing to determine processes that directly influence ice number concentrations.

We ran the same test simulations (base, HMoff, HMx5) using a development version of CAM6 (CAM6-Dev) that removes the ice number limiter from the ice nucleation scheme as described above (not shown here). Ice number concentrations in the base and HMx5 simulations are higher in CAM6-Dev compared to CESM2-CAM6 results in Figures 14 and 15. Ice number differences in CAM6-Dev are consistent with Shaw et al. (2022). Also, ice number concentrations in the HMoff simulations are lower in CAM6-Dev compared to the CESM2-CAM6. These changes result in an overall higher sensitivity to SIP in CAM-Dev. These differences are present in the

PHIPS and 2D-S size ranges. However, when we consider the detection limits of the instruments, there are no significant differences between CAM6 and CAM6-Dev mean ice number or sensitivity to HM shown in Figures 14 and 15.

Given the likely low primary ice nucleation rates from limited dust concentrations in CAM for this temperature range, it is also likely that additional processes such as sedimentation from upper level clouds and advection from surrounding grid boxes influence cloud ice concentrations. This analysis builds on previous reported assessment of IWC, which revealed a low bias in simulated IWC compared to SOCRATES observations Gettelman et al. (2020), and motivates further assessment and development of modeled secondary ice production.

8. Summary

Southern Ocean low- and mid-level clouds were investigated using an extensive in-situ payload during the SOCRATES campaign. A large fraction (45% based on the 10 s samples) of the clouds observed during SOCRATES did not contain observable amounts of ice crystals ($n_{ice} < 0.008$ L^{-1}), and thus were identified as liquid-phase. When a detectable amount of ice was present, ice crystal number concentrations up to several hundreds per liter were observed. Ice was observed in all temperatures between −25 and 0°C but the highest n_{ice} were seen around −5°C. At temperatures lower than −10°C, the observed n_{ice} were up to three orders of magnitude higher than the n_{INP} 35% of times.

The discrepancy between the observed n_{ice} and n_{INP} serves as evidence for SIP occurring in summer-time Southern Ocean stratocumulous clouds. A known SIP mechanism at temperature greater than −10°C is rime splintering in the HM process. Co-existence of large rimed ice crystals and droplets with diameters above 24 μm gave indication that rime splintering would be a possible mechanism to explain the high n_{ice} observed in the HM temperature range. However, it was found that the rate of ice production is faster than what was expected based on a conceptual model using a splinter production efficiency measured in laboratory studies (Hallett & Mossop, 1974). The frequent co-existence of large drizzle droplets with ice observations in the HM temperature regime support the hypothesis that drizzle droplets could enhance ice production rate by acting as rimers immediately upon freezing. At temperatures lower than −10°C, ice concentrations above 0.1 L^{-1} cannot be explained by primary nucleation. We report some indication of ice-ice collision and droplet shattering but the exact SIP mechanism or mechanisms acting at this temperature region remain unclear (Figure 13).

The observed n_{ice} and instrument simulators were used to evaluate simulated n_{ice} from a commonly used global climate model and to investigate the sensitivity of simulated ice concentrations to the HM process represented in CAM6. Overall, CAM6 is skilled in simulating cloud ice frequency when considering larger ice particles (200–3000 μm) at temperatures higher than −18°C, but statistically significant differences in the number concentrations of both large and small ice were observed in most of the temperature bins. Despite observational evidence of an active HM process in clouds probed during SOCRATES, simulated ice concentrations in the instrument detection range were largely insensitivity to modifications to the HM process. These results suggest that the reported low bias in simulated IWC in SOCRATES clouds Gettelman et al. (2020) may be improved with further assessment and development of modeled secondary ice production.

Appendix A: Uncertainty in Computed Number Concentrations

Cloud particle measurements have several sources of uncertainties that can affect sizing and concentration estimations. As discussed in Section 2.3.2, one of relevant source of uncertainty is shattering of larger ice crystals on the probe tips or outer structure, resulting in artificially high concentration of small crystals. During SOCRATES shattering artifacts were minimized by using anti-shattering tips for CDP, 2D-S and F-2DC and applying shattering algorithms (see Section 2.3.2). In case of PHIPS potential shattering influenced periods were identified based on presence of large ($D_a > 800$ μm) ice particles according to Waitz et al. (2021) and removed from analysis.

Besides shattering, other sources of measurement uncertainties are related to the size of the instruments' sensitive area, coincidence sampling, particle sizing and counting. The measurement uncertainties of the CDP and OAPs

have been discussed in detail by Baumgardner et al. (2017) and McFarquhar et al. (2017) and briefly summarized here for the instruments operated during SOCRATES.

In case of light-scattering probes, such as CDP, the measured number and mass concentrations are mostly affected by uncertainty in the sensitive area and coincidence sampling. The uncertainty in the CDP sensitive area has been estimated to be 13% using sensitive area mapping with a droplet injector (Lance et al., 2010), whereas the uncertainty caused by coincidence sampling can be minimized through data processing (see McFarquhar et al., 2017). It has been estimated that after data processing the remaining propagated uncertainty for derived CDP number concentration is around 10%–30% (Baumgardner et al., 2017).

In a similar manner, sample volume per unit time is needed to calculate number concentrations from OAPs. The sample volume is defined as the product of true air speed and sample area, where the sample area is defined as the product of the effective array width and separation of the instrument arms or depth-of-field (DOF), whichever is smaller (Knollenberg, 1970). The DOF is affected by light diffraction by the measured particle and is, therefore, especially uncertain for particles with $D_{max} < 150$ μm (McFarquhar et al., 2017). For larger particles, DOF is similar to the arm separation and the sample volume is less uncertain. This also supports the choice to restrict the OAP size range to particles with $D_{eq} > 200$ μm as used in this study. Additional uncertainty in DOF is caused by the nonspherical nature of ice crystals and the ambiguity in the choice for particle dimensions. The sample volume calculations are also affected by potential deviation of the true air speed at sensitive volume of the instrument from that recorded by the aircraft (Weigel et al., 2016). It is estimated that the propagated uncertainty for OAP number concentrations is around 50% for the size range used in this study (Baumgardner et al., 2017)

PHIPS particle size distribution measurements are based on single particle light scattering but instead of detecting one scattering intensity at one angular position, a set of 20 detectors with a half-opening angle of 3.5° are used covering a wider angular range from 18° to 170°. The measured differential scattering cross section corresponding to the observed angular range is then used to derive particle size. Similar to other cloud probes, the sampling rate is defined by the number of particles counted divided by the sampling volume. A separate trigger detector positioned at 90° scattering angle defines the instrument's sensitive area and, therefore, the sampling volume. The size of the PHIPS sensitive area was measured by mapping with a droplet injector (Schnaiter et al., 2018). To take into account variation in particle size and particle non-sphericity, the size- and shape-dependence of the sensitive area was simulated using a FRED optical engineering software (Waitz et al., 2021). As a result, two different functional dependencies for sensitive area as a function of particle size are used depending on the particle sphericity (phase). As a proxy for ice particles, severely roughened ice sphere model was used, as this model is independent of particle orientation. The use of a roughened ice particle model is also justified since most atmospheric ice particles have been found to be complex (Järvinen et al., 2018). However, since PHIPS is a single particle instrument, it can be expected that detected particles do have a specific orientation and a shape that can differ from that of a roughened sphere. Therefore, the measured differential scattering cross section of individual particles can be different to the modeled values, which causes uncertainty in both particle sizing and sensitive area.

In case of particle sizing, the uncertainty caused by particle shape and orientation can be estimated since PHIPS measures both the differential scattering cross section and takes stereo-microscopic images of the same particle. Figure A1 shows the relationship between D_{eq} derived from the images (defined as the mean D_{eq} from the two stereo-images) and for the same particle D_{eq} derived from the measured differential scattering cross section as defined in Waitz et al. (2021). As expected, there is a significant scatter around the 1-to-1 line, which is an effect the orientation and shape of non-spherical ice particles. The relative uncertainty in D_{eq} was estimated by binning the data to the used size bins and taking the ratio between the 25th and 75th percentiles and the median value in the bins. The resulting relative uncertainty in particle size varies between 30% and 100%.

The uncertainty in the particle sizing can be converted to an uncertainty in the sensitive area using propagation of uncertainty as these two variables are linked. Additional source of uncertainty arises from uncertainty in the spherical and aspherical particle counts caused by the phase discrimination uncertainty of 2% (Waitz et al., 2021). Furthermore, when sampling with a fast-flying aircraft, such as the HIAPER, additional sources of uncertainty are caused by compression of air in front of the cloud probe and the compression-induced motion of

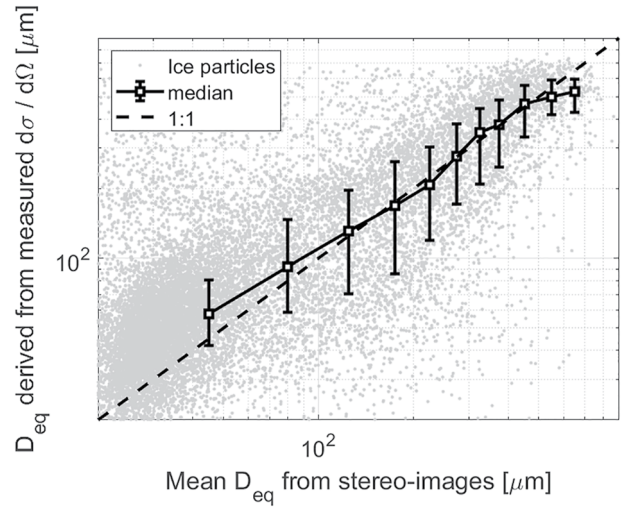

Figure A1. The relationship between D_{eq} derived from stereo-images and from the differential scattering cross section for individual oriented particles as measured during SOCRATES. The squares represent the median values in the size bins and the bars the 25th and 75th percentiles. The dashed line represent the 1:1 line.

particles out of their ambient state. Whereas the former was corrected by applying a thermodynamic correction (Weigel et al., 2016), the latter is a function of the cloud particles' individual inertia. Weigel et al. (2016) defined an inertia correction factor for droplets larger than 70 μm to be 0.8 (causing 20% reduction in the ambient number concentration compared to the measured number concentrations). Since ice crystals are expected to have lower inertia compared to more dense droplets, it can be assumed that the correction factor for $D_{eq} < 200$ μm ice particles does not significantly deviate from 1, thus being a less significant source for uncertainty compared to the other sources discussed above.

Coincidence sampling in PHIPS is possible and will mainly affect the shape of the measured angular scattering function since the forward and backward scattering detectors have a larger coincidence sampling probability than the sideward detectors. For cirrus clouds coincidence can be neglected but mixed-phase clouds have non-negligible coincidence probability (Schnaiter et al., 2018). For a particle concentration of 100 cm^{-3} the coincidence probability is 23% for the 18° and 3% for the 90° scattering detector, respectively. However, since the coincidence particles in mixed-phase clouds are most likely droplets with significant lower scattering cross section compared to ice crystals, coincidence sampling has not been seen to significantly change the shape or total intensity of the measured differential scattering cross section, and thus will probably cause a negligible uncertainty to the measurements compared to the uncertainties discussed above.

Taking into account the uncertainty in the sensitive area and particle phase discrimination, the propagated relative uncertainty in PHIPS number concentrations can be estimated. The propagated relative uncertainty depends on the number of counted particles and their size and for particles with $D_{eq} < 200$ μm, the maximum relative uncertainty in PHIPS number concentration during SOCRATES was estimated to be 40% and 20% for aspherical and spherical particles, respectively. Table A1 summarizes the uncertainties in number concentrations estimates from each of the cloud probes used in this study based on the best knowledge of the authors.

Table A1
Uncertainties in Number Concentrations Derived From CDP, 2D-S and PHIPS

Probe	Size range included into analysis	Uncertainty in number concentration
CDP	2–50 μm	~10%–30%
2D-S	200–1,600 μm	~50%
PHIPS, ice	30–200 μm	40%
PHIPS, droplets	60–700 μm	20%

Appendix B: Calculation of HM Splinter Production Rate

Willis and Hallett (1991) estimated the splinter production rate following the conceptual model by Hallett et al. (1978). In this model splinters are produced with a rate of

$$\frac{dN}{dt} = S_g N_g \tag{B1}$$

where N_g is the number concentration of graupel particles each generating S_g splinter particles per unit time. S_g can be calculated from Eq. 10 in Hallett et al. (1978).

$$S_g = N_d \alpha \pi D_g^2 V_g E/4 \tag{B2}$$

where N_d is the concentration of droplets with diameter above 24 μm, α the splinter production efficiency (measured by Hallett and Mossop (1974) to be ~0.005 with a maximum of 0.02), D_g the diameter of graupel (or rimers), V_g the fall speed of graupel (or rimers) and E the collection efficiency of the graupel (or rimers).

To calculate the splinter production rate using Equation B1 and B2 the following assumptions were made: all ice particles with $D_e > 300$ μm were assumed to be rimers, only one terminal fall velocity of 0.75 m s^{-1} was used for the rimers, the collection efficiency was assumed to be 0.8 and the splinter production efficiency 0.005.

Acronyms

2DC	The 2D Cloud Imaging probe
2D-S	The SPEC 2D stereo probe
ACE1	the First Aerosol Characterization Experiment
ASF	Angular Scattering Function
CAM6	Community Atmospheric Model versions 6
CDP	Cloud Droplet Probe
D_{eq}	Particle's Area-equivalent Diameter
D_p	Particle Diameter
DOF	Depth-of-field
Hiaper	NSF/NCAR Hiaper Gulftream GV
HM	Hallett-Mossop
INP	Ice Nucleating Particle
IS	Ice Spectrometer
IWC	Ice Water Content
LWC	Liquid Water Content
m-D	Mass to Dimension
OAP	Optical Array Probe
PHIPS	Particle Habit Imaging and Polar Scattering probe
PSD	Particle Size Distribution
RF	Research Flight
SIP	Secondary Ice Process
SO	Southern Ocean
SOCEX	the Southern Ocean Cloud Experiment
SOCRATES	the Southern Ocean Clouds, Radiation, Aerosol, Transport Experimental Study
SW	Short Wave
CWC	Condensed Water Content

Data Availability Statement

Datasets for this research are available in these in-text data citation references: Schnaiter (2018), UCAR/NCAR - Earth Observing Laboratory [EOL] (2019a), UCAR/NCAR - Earth Observing Laboratory [EOL] (2018), UCAR/NCAR - Earth Observing Laboratory [EOL] (2019b), Diao (2021), Wu and McFarquhar (2019a) and Wu and McFarquhar (2019b).

Acknowledgments
The data were collected using NSF's Lower Atmosphere Observing Facilities, which are managed and operated by NCAR's Earth Observing Laboratory (EOL). We acknowledge the help of EOL's Research Aviation Facility in campaign preparation and operations. Members of the science team who operated the instruments during the research flights are thanked. We also gratefully thank Anne Marie Rauker for assisting with processing of the INP samples. Comments from three anonymous reviewers improved the paper and are acknowledged. This material is based upon work supported by the National Center for Atmospheric Research, which is a major facility sponsored by the National Science Foundation under Cooperative Agreement No. 1852977 and under Grant No. 1660486. CSM was supported in part by the U.S. Department of Energy's Atmospheric System Research, an Office of Science Biological and Environmental Research Program, under Grant No. DE-SC0020098. KAM acknowledges support by a National Science Foundation Graduate Research Fellowship under Grant No. 006784. FW acknowledges the support of the German Research Foundation (DFG grant JA 2818/1-1). GMM acknowledges support from NSF through grants AGS-1628674 and AGS-1762096. MD acknowledges support from NSF Office of Polar Programs Grant 1744965 and the Advanced Study Program (ASP) Faculty Fellowship from the National Center for Atmospheric Research in 2018. Any opinions, findings and conclusions or recommendations expressed in this material do not necessarily reflect the views of the National Science Foundation. Open Access funding enabled and organized by Projekt DEAL.

References

Abdelmonem, A., Järvinen, E., Duft, D., Hirst, E., Vogt, S., Leisner, T., & Schnaiter, M. (2016). PHIPS–HALO: The airborne particle habit imaging and polar scattering probe – Part 1: Design and operation. *Atmospheric Measurement Techniques*, *9*(7), 3131–3144. https://doi.org/10.5194/amt-9-3131-2016

Ahn, E., Huang, Y., Chubb, T. H., Baumgardner, D., Isaac, P., De Hoog, M., et al. (2017). In situ observations of wintertime low-altitude clouds over the southern ocean. *Quarterly Journal of the Royal Meteorological Society*, *143*(704), 1381–1394. https://doi.org/10.1002/qj.3011

Atlas, R., Bretherton, C. S., Blossey, P. N., Gettelman, A., Bardeen, C., Lin, P., & Ming, Y. (2020). How well do large-eddy simulations and global climate models represent observed boundary layer structures and low clouds over the summertime southern ocean? *Journal of Advances in Modeling Earth Systems*, *12*(11), e2020MS002205. https://doi.org/10.1029/2020ms002205

Baker, B., & Lawson, R. P. (2006). Improvement in determination of ice water content from two-dimensional particle imagery. part i: Image-to-mass relationships. *Journal of Applied Meteorology and Climatology*, *45*(9), 1282–1290. https://doi.org/10.1175/jam2398.1

Baumgardner, D., Abel, S. J., Axisa, D., Cotton, R., Crosier, J., Field, P., et al. (2017). Cloud ice properties: In situ measurement challenges. *Meteorological Monographs*, *58*, 9.1–9.23. https://doi.org/10.1175/amsmonographs-d-16-0011.1

Bjordal, J., Storelvmo, T., Alterskjær, K., & Carlsen, T. (2020). Equilibrium climate sensitivity above 5 c plausible due to state-dependent cloud feedback. *Nature Geoscience*, *13*(11), 718–721. https://doi.org/10.1038/s41561-020-00649-1

Bodas-Salcedo, A., Mulcahy, J. P., Andrews, T., Williams, K. D., Ringer, M. A., Field, P. R., & Elsaesser, G. S. (2019). Strong dependence of atmospheric feedbacks on mixed-phase microphysics and aerosol-cloud interactions in hadgem3. *Journal of Advances in Modeling Earth Systems*, *11*(6), 1735–1758.

Bodas-Salcedo, A., Williams, K. D., Field, P. R., & Lock, A. P. (2012). The surface downwelling solar radiation surplus over the southern ocean in the met office model: The role of midlatitude cyclone clouds. *Journal of Climate*, *25*(21), 7467–7486. https://doi.org/10.1175/JCLI-D-11-00702.1

Boers, R., Jensen, J., & Krummel, P. (1998). Microphysical and short-wave radiative structure of stratocumulus clouds over the southern ocean: Summer results and seasonal differences. *Quarterly Journal of the Royal Meteorological Society*, *124*(545), 151–168. https://doi.org/10.1002/qj.49712454507

Boers, R., Jensen, J., Krummel, P., & Gerber, H. (1996). Microphysical and short-wave radiative structure of wintertime stratocumulus clouds over the southern ocean. *Quarterly Journal of the Royal Meteorological Society*, *122*(534), 1307–1339. https://doi.org/10.1002/qj.49712253405

Boers, R., & Krummel, P. B. (1998). Microphysical properties of boundary layer clouds over the southern ocean during ace 1. *Journal of Geophysical Research*, *103*(D13), 16651–16663. https://doi.org/10.1029/97jd03280

Braham, R. R., Jr. (1964). What is the role of ice in summer rain-showers? *Journal of the Atmospheric Sciences*, *21*(6), 640–645. https://doi.org/10.1175/1520-0469(1964)021<0640:witroi>2.0.co;2

Chubb, T. H., Jensen, J. B., Siems, S. T., & Manton, M. J. (2013). In situ observations of supercooled liquid clouds over the southern ocean during the hiaper pole-to-pole observation campaigns. *Geophysical Research Letters*, *40*(19), 5280–5285. https://doi.org/10.1002/grl.50986

Cotton, W. R., Tripoli, G. J., Rauber, R. M., & Mulvihill, E. A. (1986). Numerical simulation of the effects of varying ice crystal nucleation rates and aggregation processes on orographic snowfall. *Journal of Climate and Applied Meteorology*, *25*(11), 1658–1680. https://doi.org/10.1175/1520-0450(1986)025<1658:nsoteo>2.0.co;2

D'Alessandro, J. J., McFarquhar, G. M., Wu, W., Stith, J. L., Jensen, J. B., & Rauber, R. M. (2021). Characterizing the occurrence and spatial heterogeneity of liquid, ice and mixed phase low-level clouds over the southern ocean using in situ observations acquired during socrates. *Journal of Geophysical Research: Atmospheres*, *126*, e2020JD034482. https://doi.org/10.1029/2020JD034482

Danabasoglu, G., Lamarque, J.-F., Bacmeister, J., Bailey, D., DuVivier, A., Edwards, J., et al. (2020). The community earth system model version 2 (cesm2). *Journal of Advances in Modeling Earth Systems*, *12*(2), e2019MS001916. https://doi.org/10.1029/2019ms001916

Diao, M. (2021). Vcsel 1hz water vapor data. version 2.0. . https://doi.org/10.26023/kfsd-y8dq-yc0dAccessed 22 sep 2021.

Dye, J. E., & Hobbs, P. (1968). The influence of environmental parameters on the freezing and fragmentation of suspended water drops. *Journal of the Atmospheric Sciences*, *25*(1), 82–96. https://doi.org/10.1175/1520-0469(1968)025<0082:tioepo>2.0.co;2

Field, P., Heymsfield, A., & Bansemer, A. (2006). Shattering and particle interarrival times measured by optical array probes in ice clouds. *Journal of Atmospheric and Oceanic Technology*, *23*(10), 1357–1371. https://doi.org/10.1175/jtech1922.1

Field, P. R. (1999). Aircraft observations of ice crystal evolution in an altostratus cloud. *Journal of the Atmospheric Sciences*, *56*(12), 1925–1941. https://doi.org/10.1175/1520-0469(1999)056<1925:aooice>2.0.co;2

Field, P. R., & Furtado, K. (2016). How biased is aircraft cloud sampling? *Journal of Atmospheric and Oceanic Technology*, *33*(1), 185–189. https://doi.org/10.1175/jtech-d-15-0148.1

Field, P. R., Lawson, R. P., Brown, P. R. A., Lloyd, G., Westbrook, C., Moisseev, D., et al. (2017). Secondary ice production: Current state of the science and recommendations for the Future. *Meteorological Monographs*, *58*, 7.1–7.20. https://doi.org/10.1175/AMSMONOGRAPHS-D-16-0014.1

Fukuta, N., & Lee, H. J. (1986). A numerical study of the supersaturation field around growing graupel. *Journal of the Atmospheric Sciences*, *43*(17), 1833–1843. https://doi.org/10.1175/1520-0469(1986)043<1833:ansots>2.0.co;2

Georgakaki, P., Sotiropoulou, G., Vignon, E., Billault-Roux, A.-C., Berne, A., & Nenes, A. (2022). Secondary ice production processes in wintertime alpine mixed-phase clouds. *Atmospheric Chemistry and Physics*, *22*(3), 1965–1988. https://doi.org/10.5194/acp-22-1965-2022

Gettelman, A., Bardeen, C. G., McCluskey, C. S., Järvinen, E., Stith, J., Bretherton, C., et al. (2020). Simulating observations of southern ocean clouds and implications for climate. *Journal of Geophysical Research: Atmospheres*, *125*(21), e2020JD032619. https://doi.org/10.1029/2020JD032619

Gettelman, A., Hannay, C., Bacmeister, J. T., Neale, R. B., Pendergrass, A. G., Danabasoglu, G., et al. (2019). High climate sensitivity in the community earth system model version 2 (cesm2). *Geophysical Research Letters*, *46*(14), 8329–8337. https://doi.org/10.1029/2019gl083978

Gettelman, A., & Morrison, H. (2015). Advanced two-moment bulk microphysics for global models. part i: Off-line tests and comparison with other schemes. *Journal of Climate*, *28*(3), 1268–1287. https://doi.org/10.1175/jcli-d-14-00102.1

Gettelman, A., Morrison, H., Santos, S., Bogenschutz, P., & Caldwell, P. M. (2015). Advanced two-moment bulk microphysics for global models. part ii: Global model solutions and aerosol–cloud interactions. *Journal of Climate*, *28*(3), 1288–1307. https://doi.org/10.1175/JCLI-D-14-00103.1

Hallett, J., & Mossop, S. (1974). Production of secondary ice particles during the riming process. *Nature*, *249*(5452), 26–28. https://doi.org/10.1038/249026a0

Hallett, J., Sax, R. I., Lamb, D., & Murty, A. R. (1978). Aircraft measurements of ice in Florida cumuli. *Quarterly Journal of the Royal Meteorological Society*, *104*(441), 631–651. https://doi.org/10.1002/qj.49710444108

Haynes, J. M., Jakob, C., Rossow, W. B., Tselioudis, G., & Brown, J. (2011). Major characteristics of southern ocean cloud regimes and their effects on the energy budget. *Journal of Climate*, *24*(19), 5061–5080. https://doi.org/10.1175/2011jcli4052.1

Heymsfield, A. J., & Baumgardner, D. (1985). Summary of a workshop on processing 2-d probe data. *Bulletin of the American Meteorological Society*, *66*(4), 437–440. https://doi.org/10.1175/1520-0477-66.4.437

Hill, T. C. J., DeMott, P. J., Tobo, Y., Fröhlich-Nowoisky, J., Moffett, B. F., Franc, G. D., & Kreidenweis, S. M. (2016). Sources of organic ice nucleating particles in soils. *Atmospheric Chemistry and Physics*, *16*(11), 7195–7211. https://doi.org/10.5194/acp-16-7195-2016

Hiranuma, N., Augustin-Bauditz, S., Bingemer, H., Budke, C., Curtius, J., Danielczok, A., et al. (2015). A comprehensive laboratory study on the immersion freezing behavior of illite nx particles: A comparison of 17 ice nucleation measurement techniques. *Atmospheric Chemistry and Physics*, *15*(5), 2489–2518. https://doi.org/10.5194/acp-15-2489-2015

Hobbs, P. V., & Rangno, A. L. (1985). Ice particle concentrations in clouds. *Journal of the Atmospheric Sciences*, *42*(23), 2523–2549. https://doi.org/10.1175/1520-0469(1985)042<2523:ipcic>2.0.co;2

Hobbs, P. V., & Rangno, A. L. (1990). Rapid development of high ice particle concentrations in small polar maritime cumuliform clouds (Vol. *47*) (No. 22). https://doi.org/10.1175/1520-0469(1990)047<2710:rdohip>2.0.co;2

Hobbs, P. V., & Rangno, A. L. (1998). Microstructures of low and middle-level clouds over the beaufort sea. *Quarterly Journal of the Royal Meteorological Society*, *124*(550), 2035–2071. https://doi.org/10.1002/qj.49712455012

Holroyd, E. W. (1987). Some techniques and uses of 2d-c habit classification software for snow particles. *Journal of Atmospheric and Oceanic Technology*, *4*(3), 498–511. https://doi.org/10.1175/1520-0426(1987)004<0498:stauoc>2.0.co;2

Hoose, C., Kristjánsson, J. E., Chen, J.-P., & Hazra, A. (2010). A classical-theory-based parameterization of heterogeneous ice nucleation by mineral dust, soot, and biological particles in a global climate model. *Journal of the Atmospheric Sciences*, *67*(8), 2483–2503. https://doi.org/10.1175/2010JAS3425.1

Huang, Y., Chubb, T., Baumgardner, D., De Hoog, M., Siems, S. T., & Manton, M. J. (2017). Evidence for secondary ice production in southern ocean open cellular convection. *Quarterly Journal of the Royal Meteorological Society*, *143*(704), 1685–1703. https://doi.org/10.1002/qj.3041

Hussain, K., & Saunders, C. (1984). Ice nucleus measurement with a continuous flow chamber. *Quarterly Journal of the Royal Meteorological Society*, *110*(463), 75–84. https://doi.org/10.1002/qj.49711046307

Jackson, R. C., & McFarquhar, G. M. (2014). An assessment of the impact of antishattering tips and artifact removal techniques on bulk cloud ice microphysical and optical properties measured by the 2d cloud probe. *Journal of Atmospheric and Oceanic Technology*, *31*(10), 2131–2144. https://doi.org/10.1175/jtech-d-14-00018.1

Järvinen, E., Jourdan, O., Neubauer, D., Yao, B., Liu, C., Andreae, M. O., et al. (2018). Additional global climate cooling by clouds due to ice crystal complexity. *Atmospheric Chemistry and Physics*, *18*(21), 15767–15781. https://doi.org/10.5194/acp-18-15767-2018

Järvinen, E., Schnaiter, M., Mioche, G., Jourdan, O., Shcherbakov, V. N., Costa, A., et al. (2016). Quasi-spherical ice in convective clouds. *Journal of the Atmospheric Sciences*, *73*(10), 3885–3910. https://doi.org/10.1175/jas-d-15-0365.1

Kay, J. E., Wall, C., Yettella, V., Medeiros, B., Hannay, C., Caldwell, P., & Bitz, C. (2016). Global climate impacts of fixing the southern ocean shortwave radiation bias in the community earth system model (cesm). *Journal of Climate*, *29*(12), 4617–4636. https://doi.org/10.1175/jcli-d-15-0358.1

King, W., & Fletcher, N. (1976). Thermal shock as an ice multiplication mechanism. Part I. theory. *Journal of the Atmospheric Sciences*, *33*(1), 85–96. https://doi.org/10.1175/1520-0469(1976)033<0085:tsaaim>2.0.co;2

Knollenberg, R. G. (1970). The optical array: An alternative to scattering or extinction for airborne particle size determination. *Journal of Applied Meteorology and Climatology*, *9*(1), 86–103. https://doi.org/10.1175/1520-0450(1970)009<0086:toaaat>2.0.co;2

Koenig, L. R. (1963). The glaciating behavior of small cumulonimbus clouds. *Journal of the Atmospheric Sciences*, *20*(1), 29–47. https://doi.org/10.1175/1520-0469(1963)020<0029:tgbosc>2.0.co;2

Korolev, A., Heckman, I., Wolde, M., Ackerman, A. S., Fridlind, A. M., Ladino, L. A., et al. (2020). A new look at the environmental conditions favorable to secondary ice production. *Atmospheric Chemistry and Physics*, *20*(3), 1391–1429. https://doi.org/10.5194/acp-20-1391-2020

Korolev, A., & Leisner, T. (2020). Review of experimental studies of secondary ice production. *Atmospheric Chemistry and Physics*, *20*(20), 11767–11797. https://doi.org/10.5194/acp-20-11767-2020

Korolev, A. V., Bailey, M. P., Hallett, J., & Isaac, G. A. (2004). Laboratory and in situ observation of deposition growth of frozen drops. *Journal of Applied Meteorology*, *43*(4), 612–622. https://doi.org/10.1175/1520-0450(2004)043<0612:laisoo>2.0.co;2

Lance, S., Brock, C. A., Rogers, D., & Gordon, J. A. (2010). Water droplet calibration of the cloud droplet probe (cdp) and in-flight performance in liquid, ice and mixed-phase clouds during arcpac. *Atmospheric Measurement Techniques*, *3*(6), 1683–1706. https://doi.org/10.5194/amt-3-1683-2010

Lasher-Trapp, S., Leon, D. C., DeMott, P. J., Villanueva-Birriel, C. M., Johnson, A. V., Moser, D. H., et al. (2016). A multisensor investigation of rime splintering in tropical maritime cumuli. *Journal of the Atmospheric Sciences*, *73*(6), 2547–2564. https://doi.org/10.1175/jas-d-15-0285.1

Lasher-Trapp, S., Scott, E. L., Järvinen, E., Schnaiter, M., Waitz, F., DeMott, P. J., et al. (2021). Observations and modeling of rime splintering in southern ocean cumuli. *Journal of Geophysical Research: Atmospheres*, *126*(23), e2021JD035479. https://doi.org/10.1029/2021jd035017

Lauber, A., Kiselev, A., Pander, T., Handmann, P., & Leisner, T. (2018). Secondary ice formation during freezing of levitated droplets. *Journal of the Atmospheric Sciences*, *75*(8), 2815–2826. https://doi.org/10.1175/jas-d-18-0052.1

Lawson, P., Gurganus, C., Woods, S., & Bruintjes, R. (2017). Aircraft observations of cumulus microphysics ranging from the tropics to midlatitudes: Implications for a "new" secondary ice process. *Journal of the Atmospheric Sciences*, *74*(9), 2899–2920. https://doi.org/10.1175/jas-d-17-0033.1

Lawson, R. P., O'Connor, D., Zmarzly, P., Weaver, K., Baker, B., Mo, Q., & Jonsson, H. (2006). The 2d-s (stereo) probe: Design and preliminary tests of a new airborne, high-speed, high-resolution particle imaging probe. *Journal of Atmospheric and Oceanic Technology*, *23*(11), 1462–1477. https://doi.org/10.1175/jtech1927.1

Lawson, R. P., Woods, S., & Morrison, H. (2015). The microphysics of ice and precipitation development in tropical cumulus clouds. *Journal of the Atmospheric Sciences*, *72*(6), 2429–2445. https://doi.org/10.1175/jas-d-14-0274.1

Levin, E. J., DeMott, P. J., Suski, K. J., Boose, Y., Hill, T. C., McCluskey, C. S., et al. (2019). Characteristics of ice nucleating particles in and around California winter storms. *Journal of Geophysical Research: Atmospheres*, *124*(21), 11530–11551. https://doi.org/10.1029/2019jd030831

Liu, X., & Penner, J. E. (2005). Ice nucleation parameterization for global models. *Meteorologische Zeitschrift*, *14*, 499–514. https://doi.org/10.1127/0941-2948/2005/0059

Lloyd, G., Choularton, T., Bower, K., Crosier, J., Jones, H., Dorsey, J., et al. (2015). Observations and comparisons of cloud microphysical properties in spring and summertime arctic stratocumulus clouds during the Accacia campaign. *Atmospheric Chemistry and Physics*, *15*(7), 3719–3737. https://doi.org/10.5194/acp-15-3719-2015

Mace, G. G., Marchand, R., Zhang, Q., & Stephens, G. (2007). Global hydrometeor occurrence as observed by cloudsat: Initial observations from summer 2006. *Geophysical Research Letters*, *34*(9). https://doi.org/10.1029/2006gl029017

Mace, G. G., & Protat, A. (2018). Clouds over the southern ocean as observed from the r/v investigator during capricorn. part i: Cloud occurrence and phase partitioning. *Journal of Applied Meteorology and Climatology*, *57*(8), 1783–1803. https://doi.org/10.1175/jamc-d-17-0194.1

Mace, G. G., & Zhang, Q. (2014). The cloudsat radar-lidar geometrical profile product (rl-geoprof): Updates, improvements, and selected results. *Journal of Geophysical Research: Atmospheres*, *119*(15), 9441–9462. https://doi.org/10.1002/2013jd021374

McCluskey, C. S., DeMott, P. J., Ma, P.-L., & Burrows, S. M. (2019). Numerical representations of marine ice-nucleating particles in remote marine environments evaluated against observations. *Geophysical Research Letters*, *46*(13), 7838–7847. https://doi.org/10.1029/2018gl081861

McCluskey, C. S., Hill, T. C. J., Humphries, R. S., Rauker, A. M., Moreau, S., Strutton, P. G., et al. (2018). Observations of ice nucleating particles over southern ocean waters. *Geophysical Research Letters*, *45*(21), 11989–11997. https://doi.org/10.1029/2018gl079981

McCluskey, C. S., Hill, T. C. J., Malfatti, F., Sultana, C. M., Lee, C., Santander, M. V., et al. (2017). A dynamic link between ice nucleating particles released in nascent sea spray aerosol and oceanic biological activity during two mesocosm experiments. *Journal of the Atmospheric Sciences*, *74*(1), 151–166. https://doi.org/10.1175/JAS-D-16-0087.1

McFarquhar, G. M., Baumgardner, D., Bansemer, A., Abel, S. J., Crosier, J., French, J., et al. (2017). Processing of ice cloud in situ data collected by bulk water, scattering, and imaging probes: Fundamentals, uncertainties, and efforts toward consistency. *Meteorological Monographs*, *58*, 11.1–11.33. https://doi.org/10.1175/amsmonographs-d-16-0007.1

McFarquhar, G. M., Bretherton, C. S., Marchand, R., Protat, A., DeMott, P. J., Alexander, S. P., et al. (2021). Observations of clouds, aerosols, precipitation, and surface radiation over the southern ocean: An overview of capricorn, marcus, micre, and socrates. *Bulletin of the American Meteorological Society*, *102*(4), E894–E928. https://doi.org/10.1175/bams-d-20-0132.1

McFarquhar, G. M., Finlon, J. A., Stechman, D. M., Wu, W., Jackson, R. C., & Freer, M. (2018). University of Illinois/oklahoma optical array probe (OAP) processing software (version v3.1.4). *Zenodo*. https://doi.org/10.5281/zenodo.1285969

McFarquhar, G. M., Zhang, G., Poellot, M. R., Kok, G. L., McCoy, R., Tooman, T., et al. (2007). Ice properties of single-layer stratocumulus during the mixed-phase arctic cloud experiment: 1. Observations. *Journal of Geophysical Research*, *112*(D24). https://doi.org/10.1029/2007jd008633

Mioche, G., Jourdan, O., Delanoë, J., Gourbeyre, C., Febvre, G., Dupuy, R., et al. (2017). Vertical distribution of microphysical properties of arctic springtime low-level mixed-phase clouds over the Greenland and Norwegian seas.

Mossop, S. (1978). Some factors governing ice particle multiplication in cumulus clouds. *Journal of the Atmospheric Sciences*, *35*(10), 2033–2037. https://doi.org/10.1175/1520-0469(1978)035<2033:sfgipm>2.0.co;2

Mossop, S. (1980). The mechanism of ice splinter production during riming. *Geophysical Research Letters*, *7*(2), 167–169. https://doi.org/10.1029/gl007i002p00167

Mossop, S. (1985). Microphysical properties of supercooled cumulus clouds in which an ice particle multiplication process operated. *Quarterly Journal of the Royal Meteorological Society*, *111*(467), 183–198. https://doi.org/10.1256/smsqj.46707

Mossop, S., Ono, A., & Wishart, E. (1970). Ice particles in maritime clouds near tasmania. *Quarterly Journal of the Royal Meteorological Society*, *96*(409), 487–508. https://doi.org/10.1002/qj.49709640910

Mossop, S., Ruskin, R., & Heffernan, K. (1968). Glaciation of a cumulus at approximately- 4c. *Journal of the Atmospheric Sciences*, *25*(5), 889–899. https://doi.org/10.1175/1520-0469(1968)025<0889:goacaa>2.0.co;2

Muhlbauer, A., McCoy, I. L., & Wood, R. (2014). Climatology of stratocumulus cloud morphologies: Microphysical properties and radiative effects. *Atmospheric Chemistry and Physics*, *14*(13), 6695–6716. https://doi.org/10.5194/acp-14-6695-2014

Murphy, D. M., & Koop, T. (2005). Review of the vapour pressures of ice and supercooled water for atmospheric applications. *Quarterly Journal of the Royal Meteorological Society: A Journal of the Atmospheric Sciences, Applied Meteorology and Physical Oceanography*, *131*(608), 1539–1565. https://doi.org/10.1256/qj.04.94

Nix, N., & Fukuta, N. (1974). Nonsteady-state kinetics of droplet growth in cloud physics. *Journal of the Atmospheric Sciences*, *31*(5), 1334–1343. https://doi.org/10.1175/1520-0469(1974)031<1334:nskodg>2.0.co;2

O'Shea, S., Choularton, T. W., Flynn, M., Bower, K. N., Gallagher, M., Crosier, J., et al. (2017). In situ measurements of cloud microphysics and aerosol over coastal Antarctica during the MAC campaign. *Atmospheric Chemistry and Physics*, *17*, 13049–13070. https://doi.org/10.5194/acp-17-13049-2017

Rangno, A. L. (2008). Fragmentation of freezing drops in shallow maritime frontal clouds. *Journal of the Atmospheric Sciences*, *65*(4), 1455–1466. https://doi.org/10.1175/2007JAS2295.1

Rangno, A. L., & Hobbs, P. V. (1991). Ice particle concentrations and precipitation development in small polar maritime cumuliform clouds. *Quarterly Journal of the Royal Meteorological Society*, *117*(497), 207–241. https://doi.org/10.1002/qj.49711749710

Rangno, A. L., & Hobbs, P. V. (2001). Ice particles in stratiform clouds in the arctic and possible mechanisms for the production of high ice concentrations. *Journal of Geophysical Research*, *106*(D14), 15065–15075. https://doi.org/10.1029/2000jd900286

Rangno, A. L., & Hobbs, P. V. (2005). Microstructures and precipitation development in cumulus and small cumulonimbus clouds over the warm pool of the tropical pacific ocean. *Quarterly Journal of the Royal Meteorological Society*, *131*(606), 639–673. https://doi.org/10.1256/qj.04.13

Sassen, K. (1991). Aircraft-produced ice particles in a highly supercooled altocumulus cloud. *Journal of Applied Meteorology and Climatology*, *30*(6), 765–775. https://doi.org/10.1175/1520-0450(1991)030<0765:apipia>2.0.co;2

Schnaiter, M. (2018). Phips-halo single particle data. Version 1.0. . https://doi.org/10.5065/d6639nkqAccessed 26 nov 2018.

Schnaiter, M., Järvinen, E., Abdelmonem, A., & Leisner, T. (2018). PHIPS-HALO: The airborne particle habit imaging and polar scattering probe – Part 2: Characterization and first results. *Atmospheric Measurement Techniques*, *11*(1), 341–357. https://doi.org/10.5194/amt-11-341-2018

Shaw, J., McGraw, Z., Bruno, O., Storelvmo, T., & Hofer, S. (2022). Using satellite observations to evaluate model microphysical representation of arctic mixed-phase clouds. *Geophysical Research Letters*, *49*(3), e2021GL096191. https://doi.org/10.1029/2021gl096191

Shi, X., Liu, X., & Zhang, K. (2015). Effects of pre-existing ice crystals on cirrus clouds and comparison between different ice nucleation parameterizations with the community atmosphere model (cam5). *Atmospheric Chemistry and Physics*, *15*(3), 1503–1520. https://doi.org/10.5194/acp-15-1503-2015

Sotiropoulou, G., Vignon, É., Young, G., Morrison, H., O'Shea, S. J., Lachlan-Cope, T., et al. (2021). Secondary ice production in summer clouds over the antarctic coast: An underappreciated process in atmospheric models. *Atmospheric Chemistry and Physics*, *21*(2), 755–771. https://doi.org/10.5194/acp-21-755-2021

Stith, J. L., Ramanathan, V., Cooper, W. A., Roberts, G. C., DeMott, P. J., Carmichael, G., et al. (2009). An overview of aircraft observations from the pacific dust experiment campaign. *Journal of Geophysical Research*, *114*(D5). https://doi.org/10.1029/2008jd010924

Takahashi, T. (1993). High ice crystal production in winter cumuli over the Japan sea. *Geophysical Research Letters*, *20*(6), 451–454. https://doi.org/10.1029/93gl00613

Takahashi, T., Nagao, Y., & Kushiyama, Y. (1995). Possible high ice particle production during graupel–graupel collisions. *Journal of the Atmospheric Sciences*, *52*(24), 4523–4527. https://doi.org/10.1175/1520-0469(1995)052<4523:phippd>2.0.co;2

Trenberth, K. E., & Fasullo, J. T. (2010). Simulation of present-day and twenty-first-century energy budgets of the southern oceans. *Journal of Climate*, *23*(2), 440–454. https://doi.org/10.1175/2009jcli3152.1

Twohy, C. H., McMeeking, G. R., DeMott, P. J., McCluskey, C. S., Hill, T. C. J., Burrows, S. M., et al. (2016). Abundance of fluorescent biological aerosol particles at temperatures conducive to the formation of mixed-phase and cirrus clouds. *Atmospheric Chemistry and Physics*, *16*(13), 8205–8225. https://doi.org/10.5194/acp-16-8205-2016

UCAR/NCAR- Earth Observing Laboratory [EOL]. (2018). Ncar hsrl lidar data. version 1.0. . https://doi.org/10.5065/d6tb15r4Accessed 24 jan 2020.

UCAR/NCAR - Earth Observing Laboratory [EOL]. (2019a). Digital camera movies. version 1.0. wolff, c. [dataset]. https://doi.org/10.26023/ve64-ve6d-1z09Accessed 16 jan 2019.

UCAR/NCAR - Earth Observing Laboratory [EOL]. (2019b). Low rate (lrt - 1 sps) navigation, state parameter, and microphysics flight-level data. version 1.3. Dataset.

Vardiman, L. (1978). The generation of secondary ice particles in clouds by crystal–crystal collision. *Journal of the Atmospheric Sciences*, *35*(11), 2168–2180. https://doi.org/10.1175/1520-0469(1978)035<2168:tgosip>2.0.co;2

Waitz, F., Schnaiter, M., Leisner, T., & Järvinen, E. (2021). PHIPS–HALO: The airborne particle habit imaging and polar scattering probe – Part 3: Single-particle phase discrimination and particle size distribution based on the angular-scattering function. *Atmospheric Measurement Techniques*, *14*(4), 3049–3070. https://doi.org/10.5194/amt-14-3049-2021

Wang, Y., Liu, X., Hoose, C., & Wang, B. (2014). Different contact angle distributions for heterogeneous ice nucleation in the community atmospheric model version 5. *Atmospheric Chemistry and Physics*, *14*(19), 10411–10430. https://doi.org/10.5194/acp-14-10411-2014

Wang, Y., McFarquhar, G. M., Rauber, R. M., Zhao, C., Wu, W., Finlon, J. A., et al. (2020). Microphysical properties of generating cells over the southern ocean: Results from socrates. *Journal of Geophysical Research: Atmospheres*, *125*(13), e2019JD032237. https://doi.org/10.1029/2019jd032237

Weigel, R., Spichtinger, P., Mahnke, C., Klingebiel, M., Afchine, A., Petzold, A., et al. (2016). Thermodynamic correction of particle concentrations measured by underwing probes on fast-flying aircraft. *Atmospheric Measurement Techniques*, *9*(10), 5135–5162. https://doi.org/10.5194/amt-9-5135-2016

Willis, P. T., & Hallett, J. (1991). Microphysical measurements from an aircraft ascending with a growing isolated maritime cumulus tower. *Journal of the Atmospheric Sciences*, *48*(2), 283–299. https://doi.org/10.1175/1520-0469(1991)048<0283:mmfaaa>2.0.co;2

Woodley, W. L., Gordon, G., Henderson, T. J., Vonnegut, B., Rosenfeld, D., & Detwiler, A. (2003). Aircraft-produced ice particles (apips): Additional results and further insights. *Journal of Applied Meteorology*, *42*(5), 640–651. https://doi.org/10.1175/1520-0450(2003)042<0640:aipaar>2.0.co;2

Wu, W., & McFarquhar, G. M. (2016). On the impacts of different definitions of maximum dimension for nonspherical particles recorded by 2d imaging probes. *Journal of Atmospheric and Oceanic Technology*, *33*(5), 1057–1072. https://doi.org/10.1175/jtech-d-15-0177.1

Wu, W., & McFarquhar, G. M. (2019a). Nsf/ncar gv hiaper 2d-s particle size distribution (psd) product data. version 1.1. . https://doi.org/10.26023/8hmg-wqp3-xa0xAccessed 26 Sep 2019.

Wu, W., & McFarquhar, G. M. (2019b). Nsf/ncar gv hiaper fast 2dc particle size distribution (psd) product data. Version 1.1. . https://doi.org/10.26023/e95a-fkyf-7p0rAccessed 26 Sep 2019.

Young, G., Lachlan-Cope, T., O'Shea, S., Dearden, C., Listowski, C., Bower, K., et al. (2019). Radiative effects of secondary ice enhancement in coastal antarctic clouds. *Geophysical Research Letters*, *46*(4), 2312–2321. https://doi.org/10.1029/2018gl080551

Zhao, X., & Liu, X. (2021). Global importance of secondary ice production. *Geophysical Research Letters*, *48*(11), e2021GL092581. https://doi.org/10.1029/2021gl092581